A comparative study on deformation mechanisms, microstructures and mechanical properties of wide thin-ribbed sections formed by sideways and forward extrusion

Abstract

Extruded profiles/sections are increasingly used in the transport industry for lightweight structures. In this paper, a wide thin-ribbed aluminium profile with asymmetric Z-shape, was manufactured by a novel sideways extrusion process proposed by the authors. A comparative study was conducted by utilising the direct/forward extrusion process at the same extrusion temperature and speed, in which the different process mechanics, resulting microstructures and mechanical properties of profiles have been investigated by experiments and finite element modelling. It was revealed that, compared with sideways extrusion, although the design of a die pocket in forward extrusion induces preform and avoids the use of the large-diameter billet and extrusion container/press needed for extruding wide profiles, it requires a greater extrusion force due to work-piece upsetting necessary to fill the die pocket and leads to a lower effective strain in the profile rib. EBSD characterisation of the regions with an equal effective strain indicated that an increased shear strain is more efficient for obtaining fine grains with a higher average misorientation angle. In the same region of the profile rib made from the two different processes, sideways extrusion results in greater grain refinement due to greater effective strains, and a slightly greater texture intensity was found due to the intensive shear deformation. Tensile tests on formed profiles revealed that sideways extrusion leads to a higher yield strength (YS) and ultimate tensile strength (UTS) but a relatively lower elongation to failure, due to the combined effects of grain refinement, GND and texture intensity enhancement. Compared with the billet, the profile formed by forward and sideways extrusion has a YS increased by about 60% and 79% respectively, and an UTS increased by about 74% and 80% respectively in the extrusion direction, demonstrating an advantage of the sideways extrusion process in improving material strength under the same extrusion condition.

1. Introduction

Due to their characteristic lightweight and high stiffness/strength to weight ratio, extruded aluminium alloy profiles/sections are used to increasing extent in transport structures. They contribute to the effort to reduce structural weight and thus reduce environmentally degrading emissions from automobiles, aircraft and railway trains. Generally, a 10% weight reduction for conventional internal combustion engine (ICE) vehicles has been found to result in a 6%~8% fuel efficiency improvement [1]. With the continuously increased deployment of electrification in transportation (e-mobility), in the effort to achieve net-zero emissions by 2050, increased energy efficiency is an urgent issue in ensuring compatibility of increasing demand for electricity with available supply [2]. The potential contribution for lightweight extruded profiles in the drive to reduce vehicle weight is great and the need for new forming technologies is high [3].

Both straight and curved extruded profiles are widely used in vehicle structures. Curved profiles are generally obtained by bending forward extruded straight ones in a subsequent process. Vollertsen et al. [4] have noted that the most commonly used bending processes include rotary draw bending, roll bending, stretch bending and press bending. Generally, the force applied to bend straight extrusions tends to cause defects such as cross-sectional distortion [5], wrinkling [6, 7] and springback [8, 9]. Avoiding/eliminating these requires ad hoc methods which entail time and cost. These defects are more prevalent and of greater magnitude in thin-walled profiles, as has been described in a review by Yang et al. [10]. To deal with this problem two major research directions have emerged. One is based on refining the traditional bending process, including superposition of extra stresses [11] and torque [12], free bending with a spherical connection between the bending die and guider [13], flexible stretch bending having multiple rotational axes [14], radial hydro-forging bending where circumferential compression is applied during tube bending [15], and the recently developed

differential heating-based rotary draw bending (DH-RDB) method which contributes to breaking the forming limit of difficult-to-form tubular materials utilising neutral layer shifting reconstruction (NLSR) [16]. Another is developing integrated extrusion-bending methods, in which the profiles are bent during forward extrusion using an external deflection device such as a guiding tool [17], or bending discs [18]. Alternatively, extrusion tooling has been designed to cause unbalanced material flow across the die orifice in forward extrusion, including die orifices inclined to the punch axis [19], die land of nonuniform length [20] and punches having stepped front ends [21]. Generally, compared with the traditional bending processes, the extrusion-bending integrated methods result in improved efficiency and can reduce the bending defects caused by external bending force. For curved profile extrusion using an external deflection device, expensive and complex tooling for guiding is necessary to enable profile curvature to be changeable during extrusion. For curved profile extrusion utilising the internal differential material flow caused by design of die tooling, process flexibility is limited since profile curvature is basically pre-set or hard to be varied during the extrusion process, thus different tool designs are needed for forming profiles with variable curvatures. In addition, the mechanical properties of curved profiles formed by these processes are, at best, the same as those obtained by conventional forward extrusion.

CONFORM is a continuous extrusion process where the work-piece is pushed by frictional force from the groove wall into the stationary die channel, and extruded through an outlet either in the forward direction or perpendicular to the forward direction [22]. In the latter case the stationary die channel intersects the groove at a 90° angle, and the work-piece is subjected to a shear stress as it is forced to make a 90° turn [23]. The grain refinement induced by material flow turning an angle by shearing has long been realised, and various techniques have been developed based on this shearing. The most well-developed one is equal channel angular pressing/extrusion (ECAP/E) with the most commonly used 90° channel intersection angle [24]. To realise the continuous ECAP process, ECAP-Conform has been proposed where the work-piece experiences shearing when it turns 90° in the intersection channel of the die and groove as in the conventional ECAP [25]. Similar shearing also

3

occurs in radial extrusion where the material flows radially, i.e. perpendicular to the forward extrusion direction [26]. The CONFORM and ECAP are normally one-sided, while the radial extrusion can be one- or two-sided. Previous work on radial extrusion was conducted mostly at room temperature for simple shapes such as rods, tubes, cups, inner races, and flanges using equal ram speeds, largely demonstrating the effects of the die geometry and configuration on the shape, dimensions and flow-dependent defects of the produced parts [27-31]. Although CONFORM and ECAP/E processes utilise shear deformation to improve microstructures of materials, they cannot be applied to directly manufacture curved profiles. To enable curved profiles to be extruded directly, a novel sideways extrusion process has been proposed by the authors. In this process two opposing punches with variable velocities have been used enabling profiles with different curvatures to be produced and designed [32]. Round bars/tubes with varying curvature were manufactured, and in addition to the absence of defects and increased process efficiency resulting from integrated extrusion and bending, it was found that extrudate grain refinement occurred during sideways extrusion at room temperature due to severe plastic deformation, resulting in increased mechanical properties of AA1050 bar [33]. Sideways extrusion in general can be reasonably regarded as two equal or non-equal channel angular extrusion (N-ECAE) at the same time, depending on the location of the central dividing line determined by the velocity ratio of the two opposing punches [32]. The grain refinement during sideways extrusion utilises shearing in the intersection region of the inlet channel and the outlet channel as material flow changes 90º after extrusion, which is similar to that of channel angular extrusion [33]. However, it is realised that for the commonly used procedures for manufacturing curved aluminium alloy profiles by forward extrusion, and subsequent bending, grain refinement also occurs during the extrusion process due to dynamic recovery and dynamic recrystallization (DRX) [34]. Zhang et al. [35] studied the effects of extrusion parameters on the microstructure of AA6N01 profiles in hot forward extrusion and showed fine equiaxed grains were generated from initially coarse grains, due to dynamic recovery and DRX. Güzel et al. [36] studied the grain structure evolution along a predetermined flow line in hot forward extrusion of AA6082 at a temperature of

537 ºC, speed of 5 mm/s, and extrusion ratio of 25, it was found that the initial grain size of 110 μm was gradually refined to a size of 46 μm along the flow line, due to DRX.

For a given alloy, factors influencing the microstructure and mechanical properties of extrusion profiles include; extrusion temperature, speed (strain rate), and extrusion ratio (effective strain). Bai et al. [37] studied the effect of extrusion condition on the microstructure of a magnesium alloy (Mg-8Al-0.5Zn-0.5RE) profile and showed grain refinement occurred due to complete DRX but average size of dynamic recrystallized (DRXed) grains increased significantly with the increase of extrusion temperature. Kaneko et al. [38] investigated the forward extrusion of AZ31 at a temperature of 480 ºC and speed of 0.67 mm/s and found the grain size was refined from 24.6 μm to 13.4 μm when increasing the extrusion ratio from 4.6 to 25, and the grain was less refined at 17.0 μm with a higher extrusion speed of 2.67 mm/s. Chen et al. [39] evaluated the microstructure and mechanical properties of 2196 Al-Li alloy during hot extrusion, it was found that grain refinement increased with a proper increase of extrusion temperature and speed due to promoted degree of DRX and dynamic recovery, which also resulted in an increase of the ultimate tensile strength and yield strength of the extrudate. In view of the understanding cited above, as previous work on sideways extrusion focused on simple cross-sections formed at room temperature, to increase the applicability of the proposed sideways extrusion for manufacturing profiles, especially those with thin-walled sections, it is useful to obtain a comparison of the microstructure and mechanical properties of profiles formed by the proposed sideways extrusion with those of forward extruded profiles, at elevated temperature commonly used in industry.

In this paper, a comparison is presented of deformation mechanisms, microstructures and mechanical properties of wide thin-ribbed Z-shaped profiles formed utilising sideways and forward extrusion. To minimise the effect of bending, sideways extrusion was carried out with equal velocities of the two opposing punches so that a straight profile was produced as was that for forward extrusion. This also facilitates the cutting of samples for tensile tests and minimises the bending effect on sampling. Experiments were conducted with billets/work-pieces of commercially pure aluminium AA1100 at a

temperature of 480 ºC and a constant extrusion velocity of 0.1 mm/s. Finite element modelling was employed to facilitate understanding of the different mechanisms behind the deformation behaviour and the resulting microstructure and mechanical properties.

2. Practical experiments and process simulation

2.1. Extrusion tool design

As shown in **Fig. 1**, tool sets were made to enable both forward and sideways extrusion to be undertaken. The geometry of both die orifices and extrudate cross-sections is shown in **Fig. 1(a)**. To facilitate clarity of discussion, as shown in the figure, three parts of the cross-section across its width are referred to in the text below as, upper flange (UF), thin rib (TR), and lower flange (LF). **Fig. 1(b)** and **(c)** show the extrusion tools for forward and sideways extrusion, respectively. The tools were manufactured using H13 hot work tool steel hardened and tempered to 50 HRC. Tools with overall dimensions, 160 mm × 160 mm × 220 mm were made as two halves, to enable removal of the extrudate and remaining billet, which were clamped by high-temperature resistant bolts and nuts. The billet container diameter was 12.6 mm. For forward extrusion, as the width of the profile (23.5 mm, **Fig. 1(a)**) is greater than the diameter of the billet, a die pocket (Φ12.6 mm × 27.5 mm) was designed immediately before the die orifice, as can be seen in **Fig. 1(b)**. It should be noted that this represents a common practise in forward extrusion of wide profiles whose circumscribing circle diameter is greater than the diameter of the billet container [40-42]. Designing a die pocket can reduce the diameter of the billet needed and thus the container of the extrusion press, otherwise a much larger extrusion press is required which is not readily available [40-42]. It is realised that the geometry and size of the pocket could have an effect on metal flow [40, 43, 44], however it is out of the scope of this study. Thus the pocket was designed in such a way that its diameter was the same as that of the billet container, and its length was just a bit (2 mm) larger than the die opening/orifice on each side. For sideways extrusion, the billet was pressed simultaneously at both ends in the vertical channel of the container and extruded through the orifice of the die situated in the side of the container. The die

land/bearing for both forward and sideways extrusion dies was parallel with a length of 2 mm. In each half of the tool, 6 cylindrical holes (Φ10 mm $\times$ 210 mm) were drilled parallel to the container axis to host cartridge heaters, also, 2 cylindrical holes (Φ3 mm $\times$ 70 mm) were drilled perpendicular to the container axis to host K-type thermocouples. Both cartridge heaters and thermocouples were connected to a temperature controller through which the assembled tool was heated to a given temperature.

(b) Forward extrusion die/tooling and billet

(a) Profile (unit: mm)

(c) Sideways extrusion die/tooling and billet
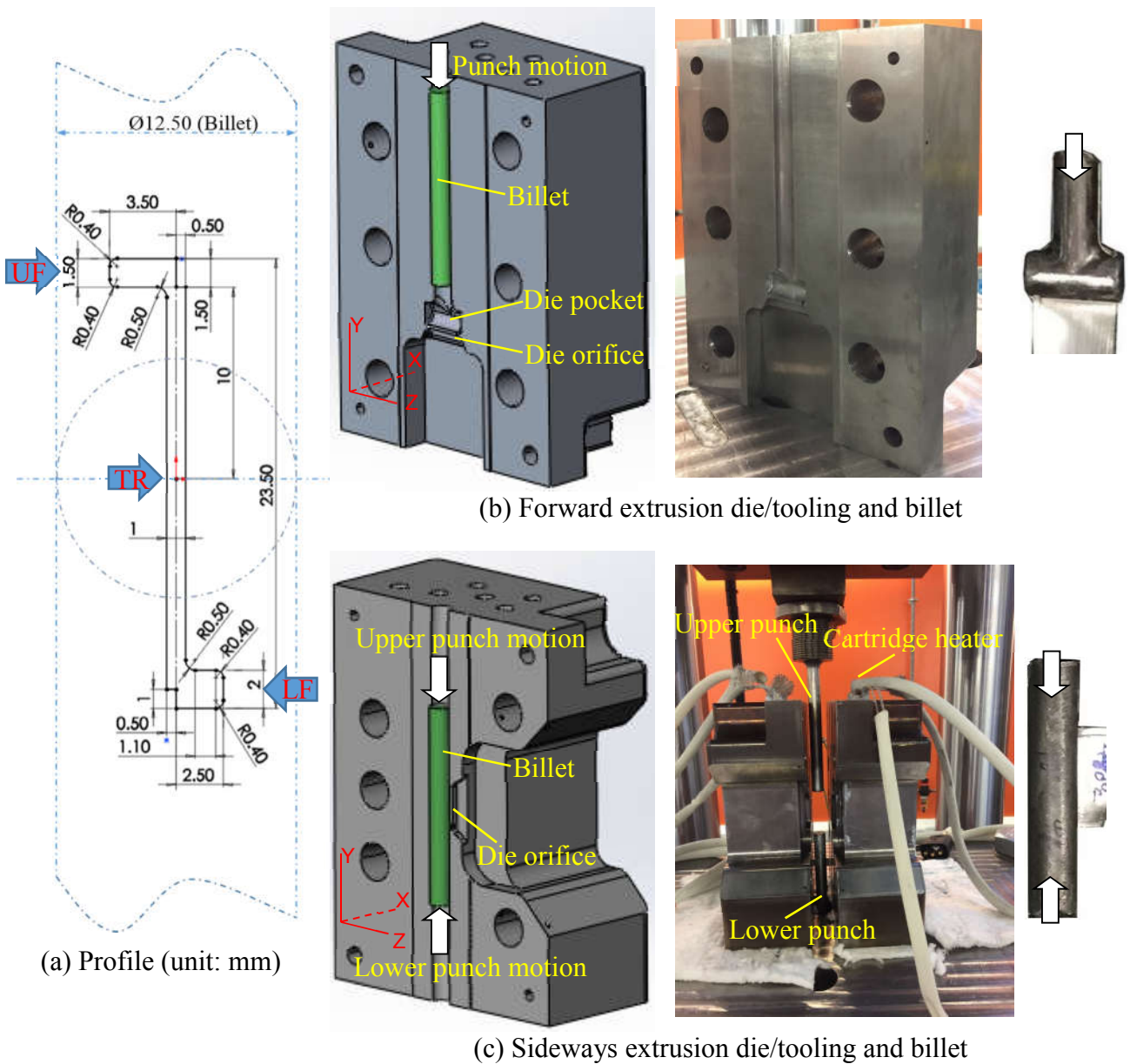
Fig. 1. (a) Geometry of the die orifice and extrudate cross-section; extrusion die/tooling and billet for (b) forward extrusion and (c) sideways extrusion.

2.2. Experimental methods

Commercially pure aluminium AA1100 was used as the test-piece material. All billets used for extrusion were prepared as cylinders whose diameter and length were 12.5 mm and 110 mm respectively. The extrusion ratio, ratio of cross-sectional area of billet to that of extrudate, was $\lambda = 3.99$ for forward and sideways extrusion, according to the traditional definition in extrusion. It should be noted that the effective extrusion ratio of the sideways extrusion process is twice the traditional extrusion ratio, because each end of the billet only forms a half of the extrudate at the equal speeds of upper and lower punches [32]. Tools were assembled with billets, punches, heaters and thermocouples and positioned in a double-acting hydraulic press. They were then heated to and held at a temperature of 480 $^{\circ}$C for 20 min to ensure temperature uniformity before extrusion at this temperature. The initial location of the billet before extrusion for sideways extrusion was symmetric to the die orifice, and for forward extrusion the billet just touched the orifice as a result of vertical extrusion, as shown in **Fig. 1(a)**. For sideways extrusion experiments, upper and lower punches were actuated simultaneously at a velocity of 0.1 mm/s. For forward extrusion experiments the single punch was actuated at a velocity of 0.1 mm/s. At the end of the extrusion process, the extrudate was cut off at the orifice within 1 min and immediately quenched in water. Samples were then extracted from quenched profiles to characterise the microstructure and mechanical properties. To study the microstructure evolution, samples were also taken from the remaining extrudate within the die for sideways and forward extrusion respectively, however, both extrudates were cooled for 12 h within the die which was unable to be dismantled at high temperature.

2.3. Numerical modelling methods

Finite element modelling using QForm-3D code was conducted in parallel with experiments to facilitate the understanding of flow patterns and plastic deformation characteristics of forward and sideways extrusion. The geometries of the finite element models were the same as those used in experiments. Billet and die were meshed with tetrahedral elements, with finer meshes in the flange

areas of die orifices. Remeshing during simulation was set with maximum steps between remeshing being 20. The material model of the extrusion tooling was H13 HRC50 and that of the billet was AA1100. The flow stress data of AA1100 imported into QForm-3D simulation is shown in **Fig. 2(a)**; it was extrapolated to a true strain of 1.5. For thermal-mechanical analysis, the relevant temperature-dependent material properties of the extrusion tooling, including Young's modulus, density, thermal conductivity, and specific heat are shown in **Fig. 2(b)-(c)**. **Table 1** is a summary of material parameters of extrusion tooling and billet material used in simulation. The heat loss as a result of convection and radiation are defined by heat transfer coefficient (HTC) and emissivity coefficient. The portion of deformation work and friction work converted into heat was considered by defining a heat generation efficiency of 0.95 for both.

The Levanov friction law was used for the friction behaviour of the extrusion tooling-billet contacting surfaces as:

$$\tau = m \frac{\sigma}{\sqrt{3}} (1 - e^{-n\frac{\sigma_n}{\sigma}})$$

where τ is friction stress, m is shear friction factor, σ is flow stress of the billet material, σ_n is normal contact pressure, and n is Levanov coefficient. The Levanov coefficient was set as 1.25 so that the Levanow friction model represents a generalisation of the Shear friction model ($\tau = m\frac{\sigma}{\sqrt{3}}$) and Coulomb friction model ($\tau = \mu\sigma_n$), where μ is friction coefficient [45, 46]. When normal contact pressure is high, i.e. large values of normal stress ratio to flow stress ($\sigma_n/\sigma > 4$), Levanov's friction stresses coincide that of the Shear friction model. When normal contact pressure is low ($\sigma_n/\sigma < 0.5$) they are close to that of the Coulomb friction model with a friction coefficient $\mu \approx 0.5$ m. Here, $m =$ 0.9 was adopted for the Levanov friction law in simulation as no lubrication was applied in extrusion practise [40]. The Coulomb friction model is solely used in QForm program for analysis of friction between tool-tool interface where no plastic deformation occurs, and $\mu = 0.3$ was set for the die-punch pair without lubricant. Finite element modelling was carried out using process parameters identical to those set in the practical tests enabling modelling results and the test data to be compared.
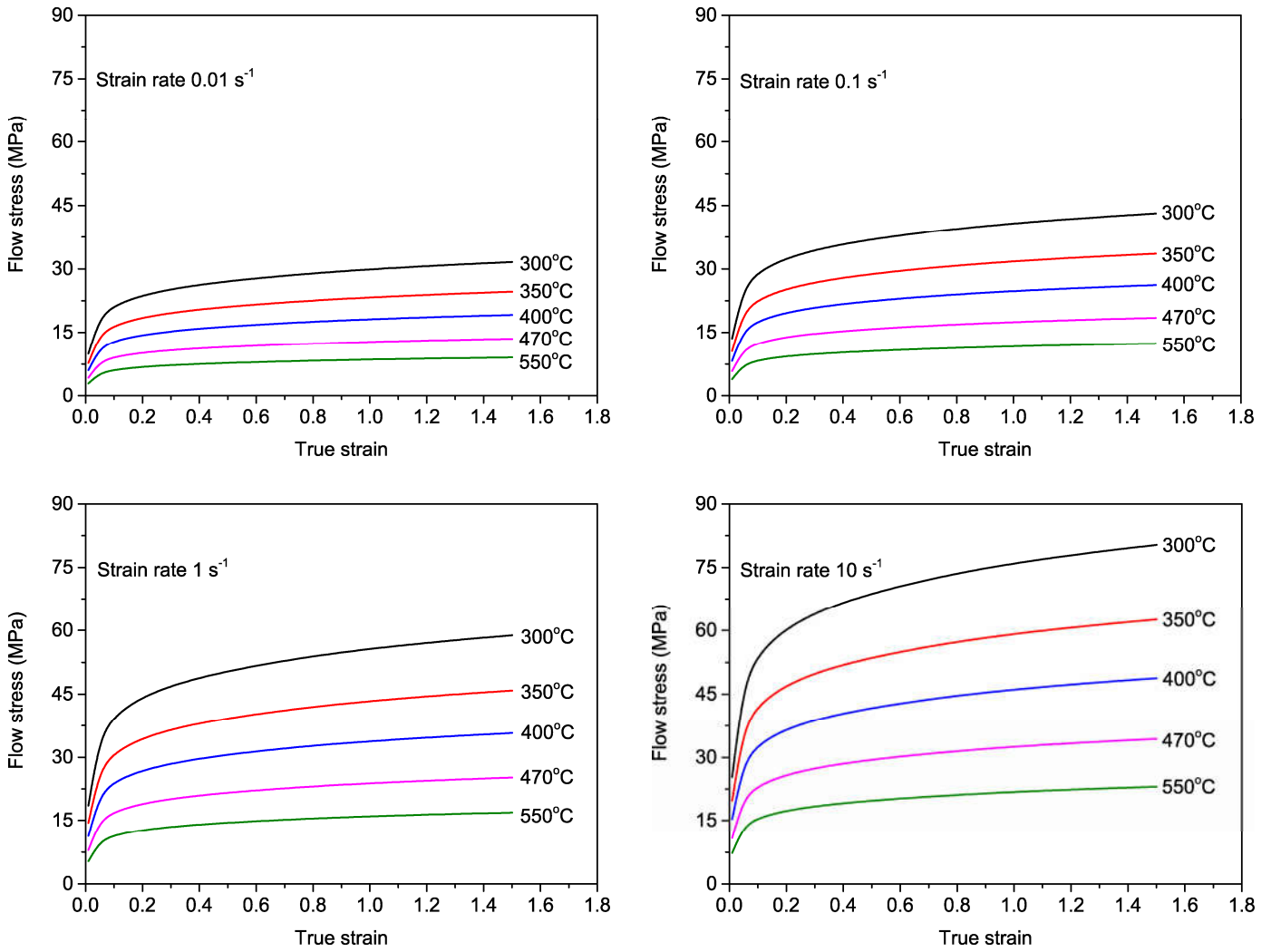
(a) Flow stress data of AA1100
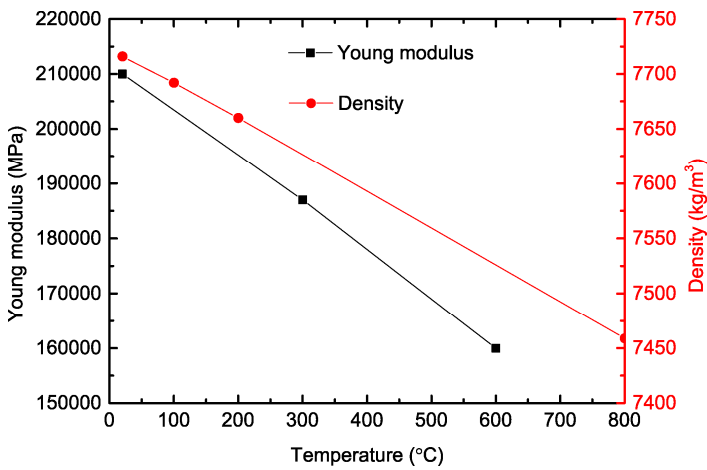
(b) Young's modulus and density
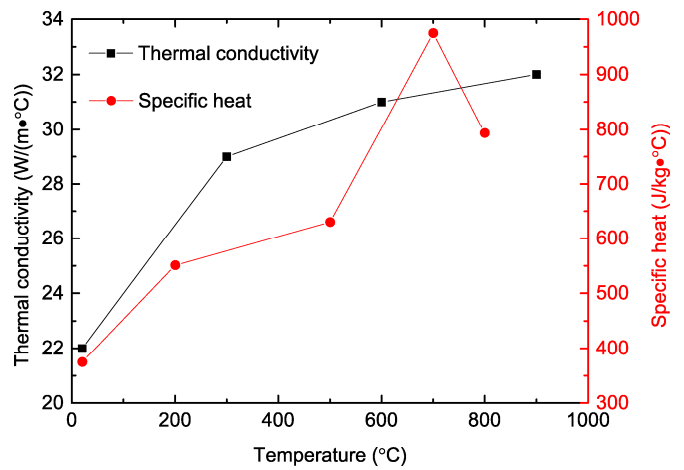
(c) Thermal conductivity and specific heat

Fig. 2. Material properties of the billet and extrusion tooling: (a) true stress-strain curves of the billet alloy, (b) Young's modulus and density of extrusion tooling, (c) thermal conductivity and specific heat of extrusion tooling.

Table 1. Material properties of the billet and extrusion tooling.

Property	Billet	Extrusion tooling
Material	AA1100	H13 tool steel (HRC50)
Density (kg/m^3)	2640	Fig. 2(b)
Young's modulus (MPa)	-	Fig. 2(b)
Poisson's ratio	0.33	0.30
Thermal conductivity (W/(m·^{o}C))	226	Fig. 2(c)
Specific heat (J/(kg·^{o}C))	930	Fig. 2(c)
Heat transfer coefficient between tooling and billet (W/(m^2·^{o}C))	11000	11000
Heat transfer coefficient between tooling/billet and air (W/(m^2·^{o}C))	20	20
Emissivity coefficient	0.7	0.7

2.4. Microstructural characterisation and mechanical property tests

A Bruker's QUANTAX electron backscatter diffraction (EBSD) device was used to characterise the microstructure of the formed profiles. **Fig. 3(a)** illustrates the sampling orientation. Zones F_f, Fc from a forward extruded profile, and zones S_f, Sc from a sideways extruded profile, which are close to the die orifice and in the flow plane ED-ND (F_f, S_f) and cross-sectional plane TD-ND (Fc, Sc) respectively, were taken for EBSD characterisation. The EBSD device was mounted on a Hitachi S-3400N SEM with an operation voltage of 20 kV. The preparation of samples follows conventional metallographic procedures, including cold mounting, grinding and polishing. Conductive resin Demotec 70 was used to cold mount the samples at room temperature, and grinding was carried out with silicon carbide papers (grit 600, 800, 1200 and 4000). Polishing was firstly conducted on Metprep® Alpha cloth, where 1 μm diamond polishing solution and water-based lubricant were used, followed by 0.04 μm colloidal silica solution. Then samples were argon ion polished on a GATAN PECS II device. Tensile tests were performed at room temperature on a Deben MICROTEST tensile stage at a speed of 0.4 mm/min. Specimens, with gauge sections of 1 mm × 2.5 mm × 5 mm, as shown in **Fig. 3(b)**, were cut from the profiles along the extrusion direction (ED) and normal direction (ND).

(a) EBSD sampling location and orientation   (b) Tensile sample
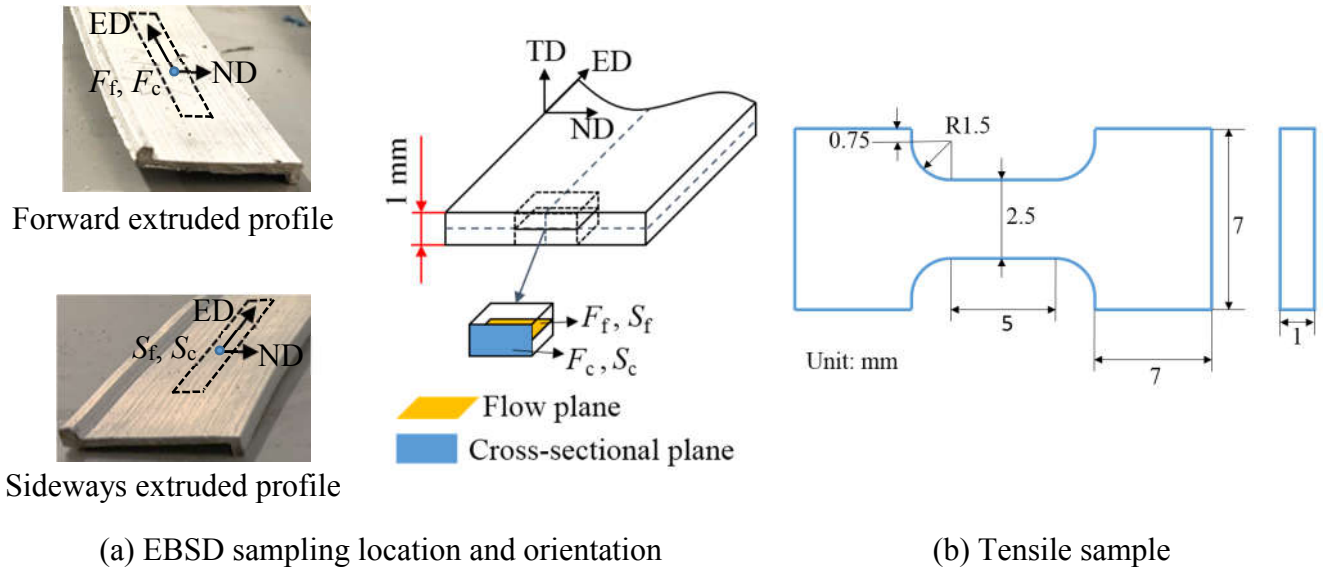
Fig. 3. Locations and orientations of zones F_f, Fc and S_f, Sc for EBSD characterisation, and dimensions of tensile samples cut from the profiles.

3. Results and discussion

3.1. Comparison of the extrusion load, dead zone and flow pattern

The finite element model was firstly validated by comparing the profile geometry and load-time curve for sideways extrusion obtained from experiments and modelling, as shown in **Fig. 4.** It can be seen that both of the profiles are slightly bent towards the upper flange. Probably this is due to the fact that although this flange is thinner than the lower one, 1.5 mm compared with 2 mm (**Fig. 1(a)**), it has a bigger cross-sectional area, 5.25 mm^2 compared with 5 mm^2, and its lesser effective extrusion ratio would have resulted in slightly slower extrudate flow. Also, the metal in the upper flange has a greater flow resistance caused by the friction due to a greater contact area between the work-piece and die. The steady-state load obtained by modelling is about 10% lower than the experimental one. The discrepancies in the profile geometry and extrusion force obtained from experiments and modelling might be attributed to the difference between the friction conditions in experiments and modelling. The load-time curve for forward extrusion is shown in **Fig. 5**, which was extracted from simulated results. Its stepped rise indicates a two-stage process. The first stage relates to the filling of the pre-orifice pocket under near constant load followed by a rapidly increasing load as extrusion through the

orifice occurs. Specifically, in the first stage, load increases steadily and slowly until the billet reaches the two ends of the die pocket (load 16.0 kN). At this stage, the left and right corners of the two ends have not yet been filled. Also, a very small amount of material has entered the die land/bearing (thin rib). In the second stage, load increases dramatically, where firstly the four corner gaps are filled (load 23.5 kN) with a small amount of alloy entering both the thin rib and upper and lower flanges of die land/bearing, then the die land is completely filled and complete cross-sections emerge at a peak load of 27.0 kN. After reaching the peak load, the load for both forward and sideways extrusion processes gradually decrease with further extrusion as billet length and hence total friction force decreases. It can also be seen that inclusion of a pocket in the forward extrusion process results in a larger peak force requirement, compared with that for the sideways extrusion process.



| (a) Profile geometry | (b) Load-time curve |
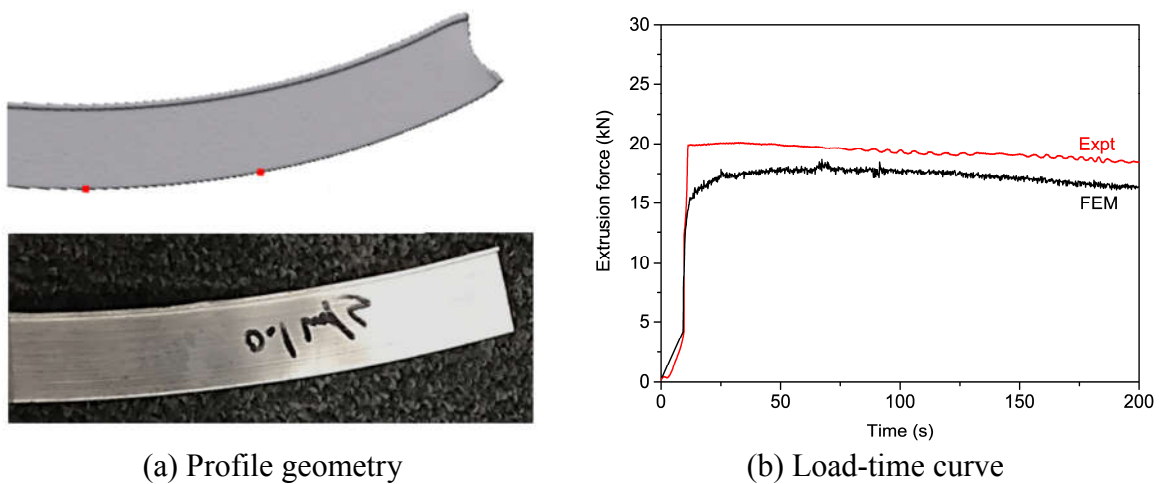
Fig. 4. Comparison between experimental and simulation results for sideways extrusion.
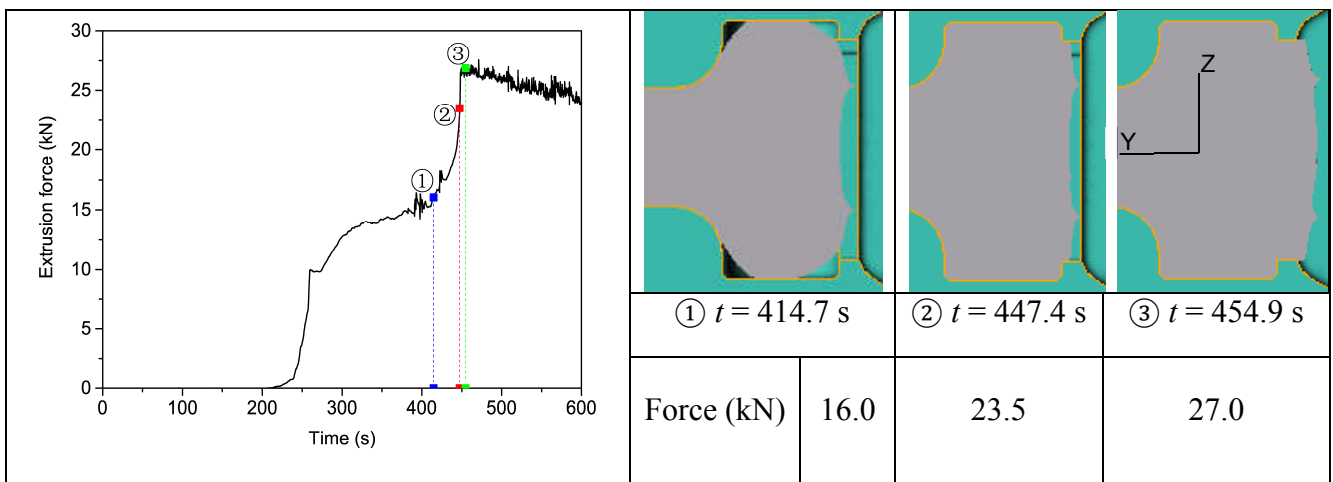
Fig. 5. Load-time curve and forming stages in forward extrusion.

13

Simulated velocities on the symmetric flow plane *Y-Z* of the billet are shown in **Fig. 6**. The velocities in the punch movement direction (-*Y* for forward extrusion, ±*Y* for sideways extrusion) and the direction *Z* perpendicular to punch movement, are shown for forward extrusion in **Fig. 6(a)** and **(b),** and sideways extrusion in **Fig. 6(c)** and **(d)**. Here the scale bars have been manually adjusted for highlighting the dead metal zone (DMZ), a velocity of absolute value 0.005 mm/s is used to define the upper flow limit of material in dead zones. It should be noted that the maximum velocity of material out of dead zones is much larger than the maximum value shown in the scale bars. As shown in **Fig. 6(a)** and **(b)**, for forward extrusion, two dead metal zones of right triangular shapes occur in the 90 degree corners of the die pocket opposite the die orifice; the billet in these zones has a negligible velocity of about 0.001 mm/s in both *Y* and *Z* directions. The other two 90 degree corners of the die pocket do not contain obvious dead metal zones possibly because they are influenced by their proximity to the die orifice. For sideways extrusion, as shown in **Fig. 6(c)** and **(d)**, a dead metal zone of roughly triangular shape, smaller than that found in forward extrusion, exists on the chamber wall opposite and central to the die orifice. Similar to the forward extrusion process, alloy in this zone has a negligible velocity of about 0.001 mm/s in both *Y* and *Z* directions. It can also be seen that a line dividing the deformation zone and die orifice into two parts can be drawn in **Fig. 6c,** which passes through the vertex of the DMZ. The extrudate consists of equal parts of alloy moving in opposite directions within the billet chamber. The flow dividing line lies in the centre of the deformation zone and die orifice as the upper and lower punches have the same speed. This phenomenon has also been identified in previous experimental and theoretical studies on bar and tube forming in the sideways extrusion process [47, 48].
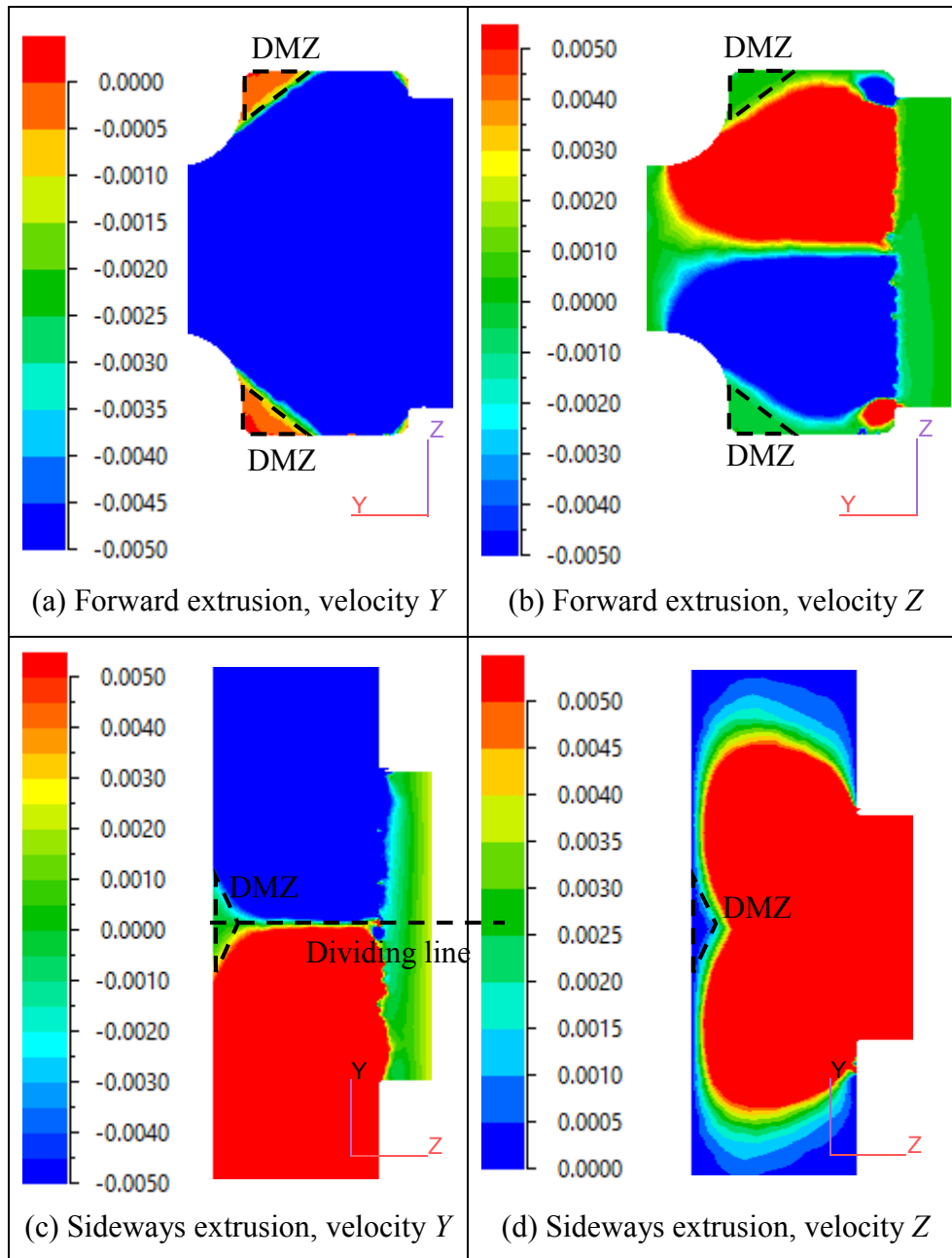
Fig. 6. Flow velocities (mm/s) highlighting dead metal zones for forward and sideways extrusion.

Flow lines and mesh grids, on the symmetric flow plane *Y-Z*, obtained from modelling forward and sideways extrusion are shown in **Figs. 7** and **8** respectively. **Fig. 7(a)** shows the stage of forward extrusion at time *t* = 452.4 s, when the pocket is filled and extrusion is about to start. It can be seen that the grids in the central region of the pocketed metal are severely compressed in the direction *Y* and pocket corners have been filled by shearing of metal. **Fig. 7(b)-(e)** show stages of forward extrusion at *t* = 498.6 s, 526.5 s, 559.0 s, and 594.9 s, sequentially. It can be seen that as extrusion continues, grids in the central region of the pocket metal become stretched in both *Y* and *Z* directions

as they approach and pass through the die orifice. **Fig. 7(f)** shows the stage of steady forward extrusion at $t = 674.6$ s. The extrudate length is about 85 mm. It can be seen that at this steady-state stage, longitudinal grid lines are parallel after exiting the die orifice.
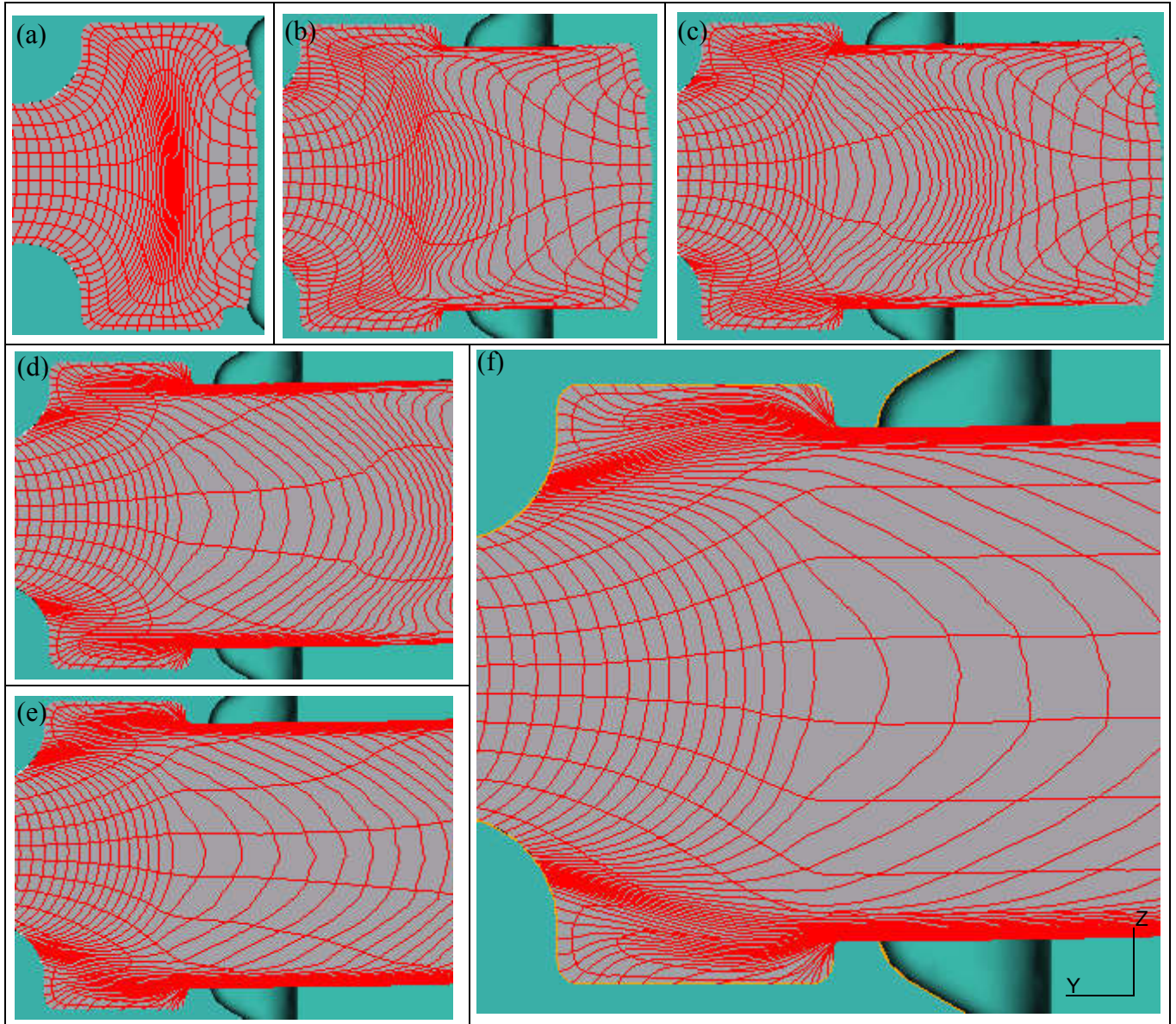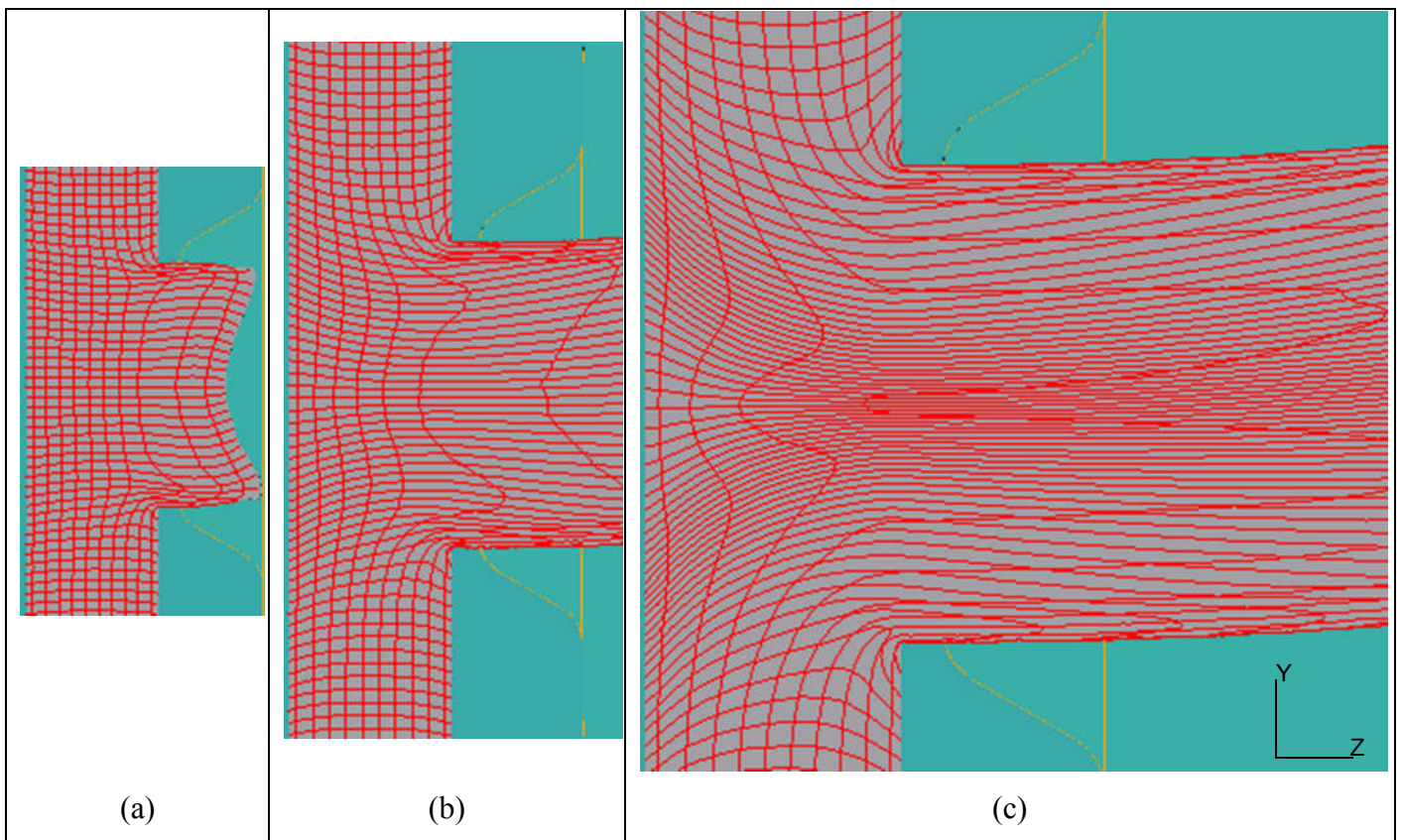

Fig. 7. Flow lines and mesh grid distortion for forward extrusion at different stages: (a) $t = 452.4$ s, (b) $t = 498.6$ s, (c) $t = 526.5$ s, (d) $t = 559.0$ s, (e) $t = 594.9$ s, (f) $t = 674.6$ s.

Fig. 8(a) shows, at the early stage of sideways extrusion ($t = 19.8$ s), metal in regions of upper and lower flanges flows faster than that of the thin rib. **Fig. 8(b)** shows the stage when upper and lower punch forces reach peak values ($t = 48.5$ s). The shape of the transverse grids reveals flow is faster in the region of the lower flange than the upper one. This is also shown by the slight bending of profiles

16

towards the upper flange in **Fig. 4**, and is probably due to the greater area of work-piece die contact and lower effective extrusion ratio for the upper flange. **Fig. 8(c)** shows the stage of sideways extrusion at t = 139.0 s. It indicates that except for the dead metal zone, the longitudinal billet grids rotate through 90º to enter the die orifice. Grids in the extended dividing line of the dead metal zone are compressed by the punches, then elongated along the extrudate. Grids transverse to extrudate length exist largely in this narrow central region, compared with those extending across the width of the forward extruded extrudate. The aspect ratios of grids at the die orifice of **Fig. 8(c)** are significantly greater than those of **Fig. 7(f)**.

Fig. 8. Flow lines and mesh grid distortion for sideways extrusion at different stages: (a) t = 19.8 s, (b) t = 48.5 s, (c) t = 139.0 s.

It is found from the above simulated results that there are typical shearing bands for both the sideways and forward extrusion. Grenerally, the appearance of shearing bands during the forming process might induce ductile fracture due to the large deformation. **Fig. 9** shows the etched extrudeates cut from the symmetric flow plane *Y-Z*, which are compared with the simulated flow patterns. The

shearing bands and flow patterns shown in the simulation can be roughly identified from the etched results. In addtion, no fracture or damage in the extrudates was observed. This is probably due to the elevated forming temperature where the aluminium has high ductility and low deformation resistance, which is the typical temperature used in industrial practice for extruding complex profiles.

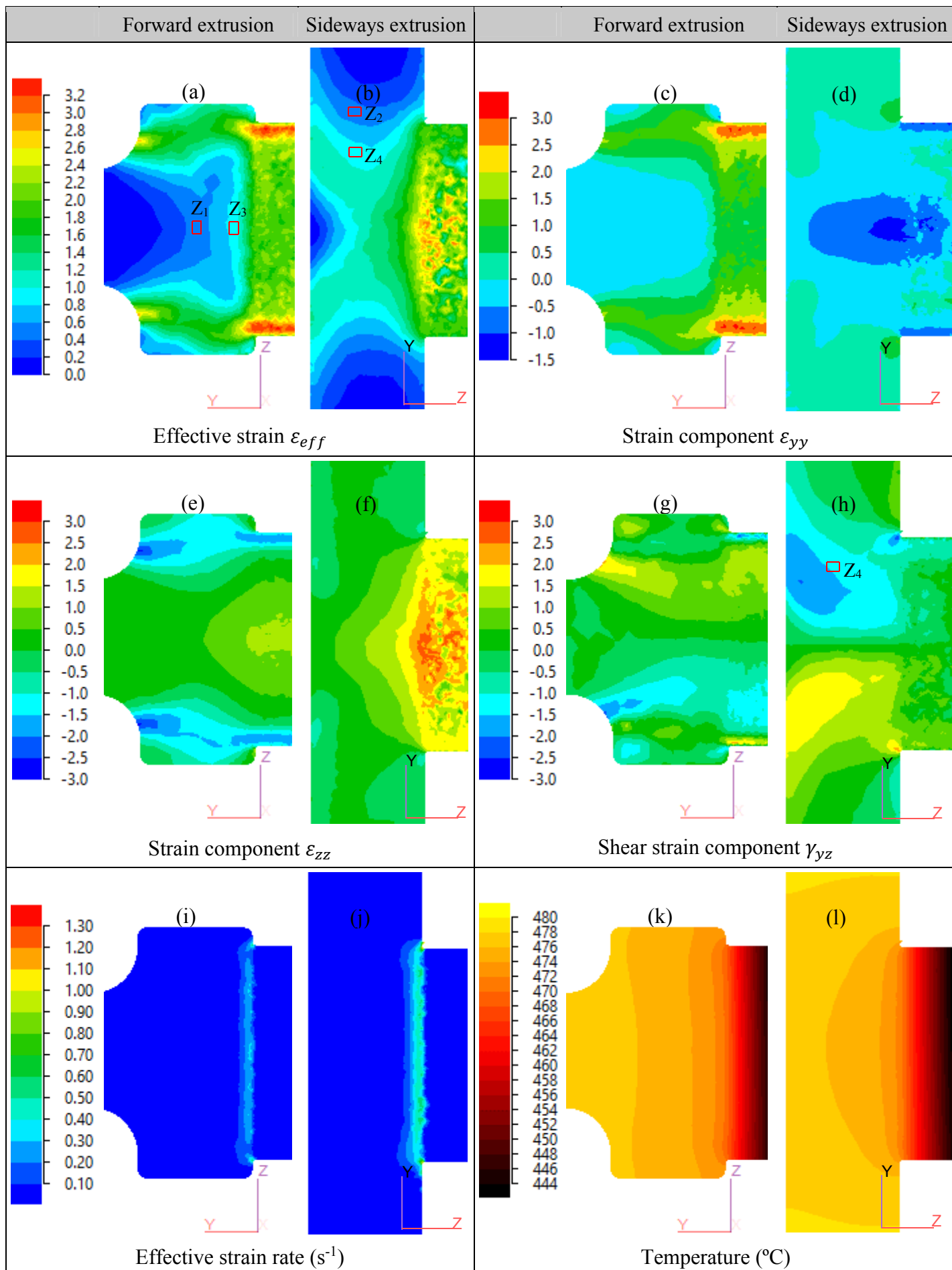| (a) Forward extrusion | (b) Sideways extrusion |
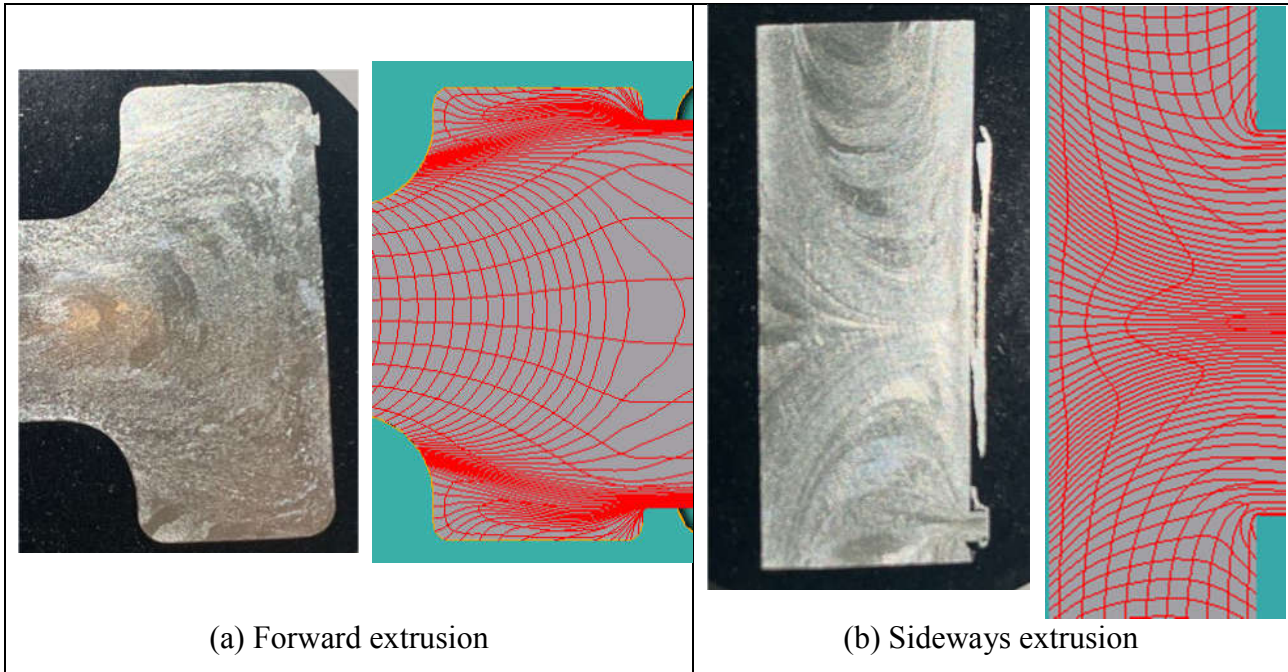
Fig. 9. Comparison of flow patterns in the symmetric flow plane for (a) forward and (b) sideways extrusion. The left column indicates etched results, the right column indicates simulated results.

3.2. Comparison of the strain, strain rate and temperature fields

Fig. 10(a) and **(b)** show effective strain contours for forward extrusion and sideways extrusion at a steady-state stage, for an extrudate length of about 85 mm. The sideways extruded extrudate has experienced a lower effective strain level in the flanges and greater effective strain level in the thin rib compared with that resulting in the forward extruded extrudate. For sideways extrusion the highest value of effective strain occurs in the mid-width region of the extrudate where the flow dividing line lies, for forward extrusion the highest value of effective strain lies in the extrudate flanges. This difference reflects the mesh grid distortion shown in **Figs. 7** and **8** and is further demonstrated by examining the strain components in **Fig. 10(c)-(h)**.

For forward extrusion, a relatively large-area, uniform compression zone of small value exists in the centre of the die pocket, along the extrusion direction Y (**Fig. 10(c)**). Meanwhile, due to upsetting in the pocket, relatively uniform but small-valued tension exists in the direction Z perpendicular to extrusion (**Fig. 10(e)**), which gradually turns into severe compression at the upper and lower ends of the die pocket due to constraint of the pocket wall. As metal passes through the die orifice, compression along the extrusion direction Y, gradually changes to tension (**Fig. 10(c)**), and tension in the direction Z perpendicular to extrusion greatly increases (**Fig. 10(e)**). Two significant shearing zones exist, one at the intersection of the upper billet half and die pocket (positive shearing), the other at the intersection of the lower billet half and die pocket (negative shearing), as shown in **Fig. 10(g)**.

For sideways extrusion, the compressive strain along the punch movement direction Y, gradually increases towards the central dividing line, as shown in **Fig. 10(d)**. The peak value is more severe compared with the compressive strain in the extrusion direction Y of forward extrusion (**Fig. 10(c)**). As shown in **Fig. 10(f)**, the tensile strain in the direction Z, perpendicular to punch movement, gradually increases towards the die orifice where the greatest tensile strain occurs in the dividing line of the die orifice. Again, the peak value is more severe than the tensile strain in the direction Z for forward extrusion (**Fig. 10(e)**). Two shearing zones exist in the intersection region of the billet and die orifice, as shown in **Fig. 10(h).** The peak values of shear strain are around the corners of the flow dividing line and billet surface (above the DMZ) and are much greater than that for forward extrusion (**Fig. 10(g)**). The shearing in sideways extrusion is similar to the severe shear deformation arising in the intersection region of the equal or non-equal channel angular extrusion/pressing (ECAE/P or NECAE/P) [49, 50]. Overall, the effective strain in the thin rib region of the extrudate made by sideways extrusion is greater than that in the extrudate made by forward extrusion. The three strain components in the flanges are greater for the forward extruded extrudate than for the sideways extruded one, resulting in a greater effective strain in the flanges of the former part.

| Forward extrusion | Sideways extrusion | | Forward extrusion | Sideways extrusion |

(a) (b) Effective strain ε_{eff}

(c) (d) Strain component ε_{yy}

(e) (f) Strain component ε_{zz}

(g) (h) Shear strain component γ_{yz}

(i) (j) Effective strain rate (s^{-1})

(k) (l) Temperature ($^{\circ}$C)

Fig. 10. Strain, strain rate and temperature fields on the symmetric flow plane *Y-Z* of forward and sideways extrusion at a steady-state stage for the same length of extrudate: (a)-(b) effective strain ε_{eff}, (c)-(d) normal strain component ε_{yy}, (e)-(f) normal strain component ε_{zz}, (g)-(h) shear strain component γ_{yz}, (i)-(j) effective strain rate (s^{-1}), (k)-(l) temperature (ºC). The left column indicates forward extrusion, the right column indicates sideways extrusion.

Fig. 10(i) and **(j)** allow comparison of effective strain rate contours in forward and sideways extruded extrudates of the same length as those in **Fig. 10(a)-(h)**. It can be seen that the maximum effective strain rate occurs at the die orifice for both forward and sideways extrusion, however the effective strain rate for sideways extrusion is much greater than that for forward extrusion, because each end (upper end or lower end) of the billet only forms a half of the extrudate (i.e. the effective extrusion ratio of sideways extrusion is greater than the traditional one), as shown in **Fig. 8**. **Fig. 10(k)** and **(l)** show respectively the corresponding temperature field for forward and sideways extrusion. It can be seen that temperature has a similar distribution for forward and sideways extrusion. Due to the relatively low extrusion speed of 0.1 mm/s, and modest extrusion ratio, temperature rise due to heat of deformation is not significant. A gradual decrease in billet temperature occurs as it approaches the die orifice due to heat transfer to air, and the extrudate temperature drops steadily as it moves away from the die orifice.

3.3. Comparison of the microstructure and mechanical properties

3.3.1. Microstructure

Four different zones, Z_1-Z_4 as marked in **Fig. 10**, were carefully selected to compare the different microstructural evolution within the die. The deformation and related microstructure characteristics of these zones are given in **Table 2**. The strain values were taken from the centre of each zone. Z_1 and Z_2 (or Z_3 and Z_4) have the same effective strain but their shear and normal strains are very different. The shear strain and normal strain respectively dominates the effective strain for sideways extrusion (Z_2 and Z_4) and forward extrusion (Z_1 and Z_3). **Fig. 11** shows the obtained EBSD maps of Z_1-Z_4. The

white line indicates the low angle boundaries (LABs, misorientation angle $2° \leq \theta < 15°$) and the black line indicates the high angle boundaries (HABs, misorientation angle $\theta \geq 15°$). The initial AA1100 billets had cast coarse grains with an average grain size of ~ 600 μm. **Fig. 11(a)** and **(b)** show that at an effective strain of 0.5, large fractions of subgrains have been generated inside the initial coarse grains, but the average misorientation angle and the fraction of HABs are higher for sideways extrusion than forward extrusion. This could be due to the different values of shear and normal strains. The shear strain contributes to the increasing of average misorientation angle. This phenomenon becomes more obviously seen in **Fig. 11(c)** and **(d)** which have a higher same effective strain and greater difference between shear strains. **Fig. 11(c)** shows the initial coarse grains for forward extrusion are further compressed in the extrusion direction Y and elongated in the direction Z perpendicular to extrusion at an effective strain of 0.9. With the increase of the effective strain, the fraction of new grains with HABs increases, leading to an increase of the average misorientation angle and grain refinement. Similar but stronger tendencies have been found for sideways extrusion, as shown in **Fig. 11(d).** Grain structure becomes band-like and develops a high aspect ratio lamellar HABs structure ~ 45° to extrusion. Higher misorientation angles have been developed within the band-like structures, leading to a more refined microstructure with higher average misorientation angle, compared with forward extrusion shown in **Fig. 11(c)**. Thus, it is obvious that for the same effective strain increment, the increase of the misorientation angle is more prominent in sideways extrusion than that in forward extrusion.

It can also be seen in **Fig. 11(d)** that a gradient structure exists from the top right corner to bottom left corner, where the fraction of fine recrystallized grains with HABs gradually increases within shearing bands. The width of shearing bands tends to decrease as well. This could be due to the slight gradient variation of strain towards the bottom left corner. The specific distribution of misorientation angle for different subzones (I, II and III in **Fig. 11(d)**) is shown in **Fig. 12(a)**, the corresponding strain variation is shown in **Fig. 12(b)**. It can be seen that the effective strain remains nearly the same, while the absolute value of the shear strain gradually increases from subzone I to subzone III,

accompanied by a slight decrease of all three normal strain components. A finer lamellar grain structure with higher degree of misorientation is formed in subzone III which has a higher shear strain. The above results indicate that shearing is more effective in increasing misorientation angles than normal strain components, an increased shear strain is more efficient for obtaining fine grains under the fixed effective strain.

Table 2. Comparison of microstructural features in different zones of forward and sideways extrusion with equal effective strains.

	ε_{eff}	γ_{yz}	ε_{yy}	ε_{zz}	ε_{xx}	Average misorientation angle $\bar{\theta}$ (°)	Fraction of HABs f_{HABs} (%)
Z_1 (Forward extrusion)	0.5	0	-0.38	0.45	-0.07	6.66	5.38
Z_2 (Sideways extrusion)	0.5	-0.80	-0.05	0.13	-0.14	9.78	15.76
Z_3 (Forward extrusion)	0.9	0	-0.33	0.87	-0.54	10.18	17.53
Z_4 (Sideways extrusion)	0.9	-1.42	-0.15	0.29	-0.20	16.20	30.39

(a) Z_1 (Forward extrusion)

(b) Z_2 (Sideways extrusion)

(c) Z_3 (Forward extrusion)

(d) Z_4 (Sideways extrusion)
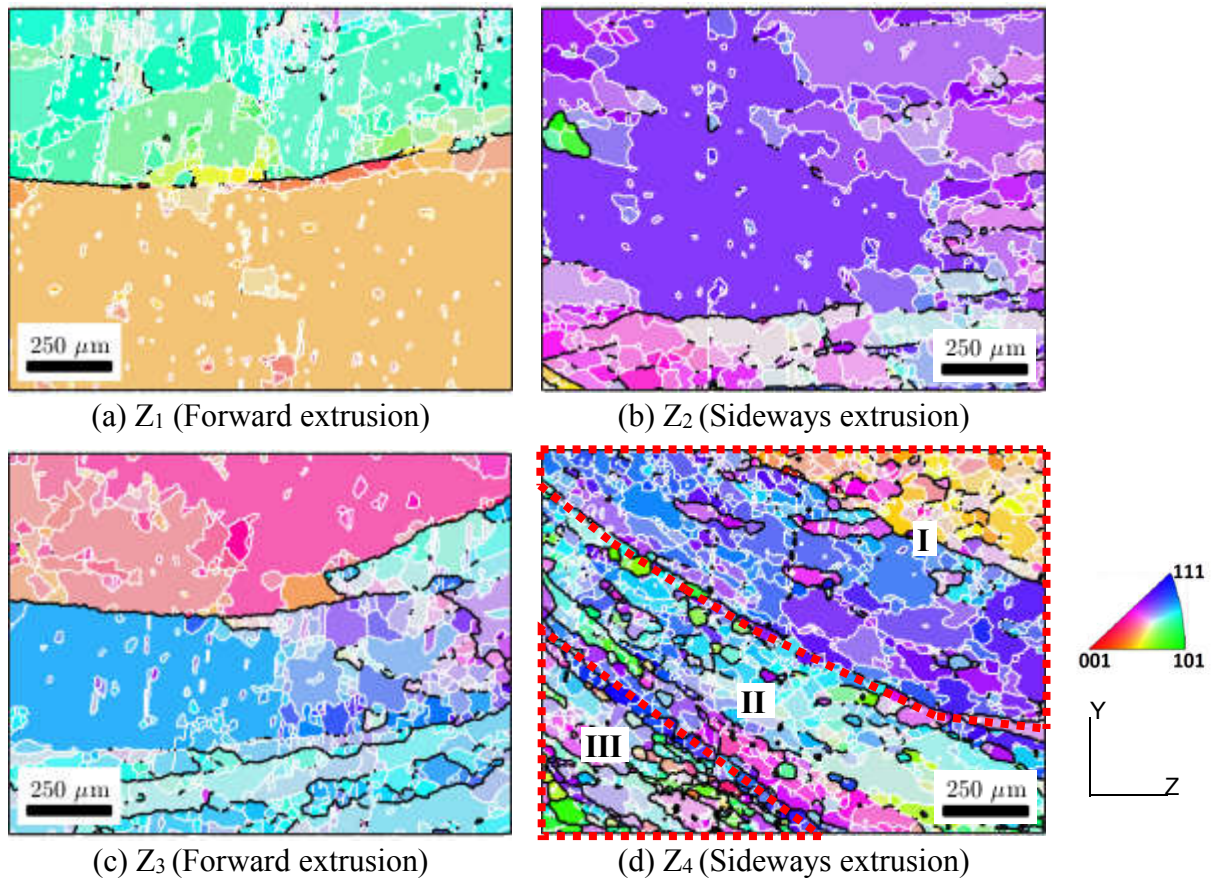
Fig. 11. EBSD inverse pole figure (IPF) maps at selected zones of forward and sideways extrusion with equal effective strain ε_{eff}: (a)-(b) $\varepsilon_{eff} = 0.5$, (c)-(d) $\varepsilon_{eff} = 0.9$.

(a) Misorientation angle (b) Deformation characteristics
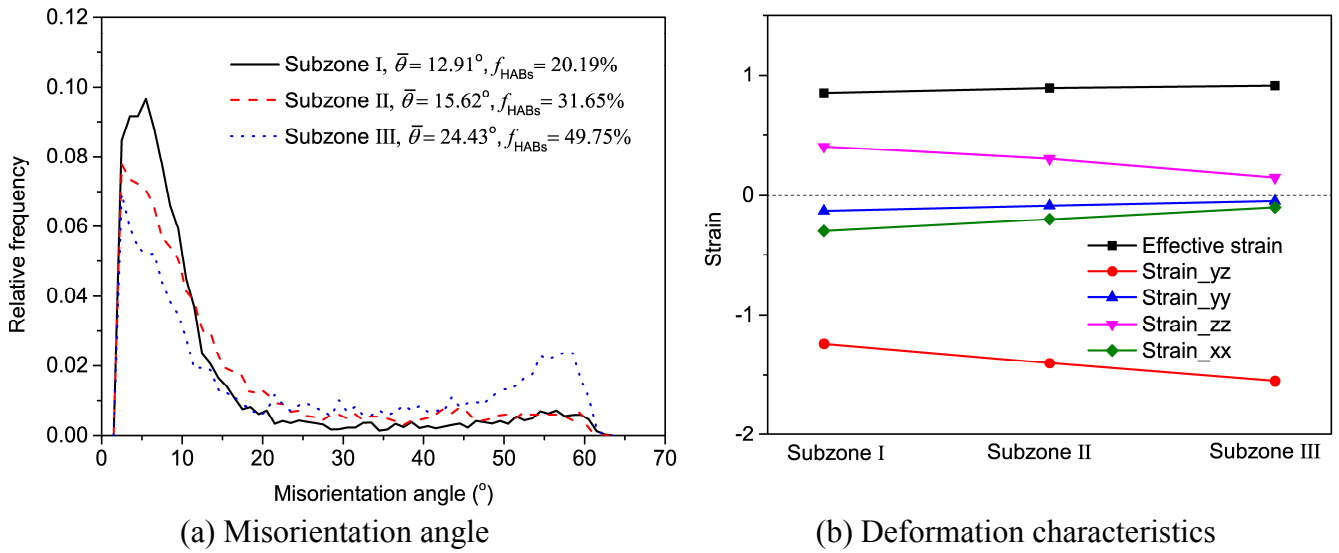
Fig. 12. Misorientation and deformation characteristics in selected subzones of Z_4.

To compare microstructures in formed profiles, zones F_f, Fc and S_f, Sc shown in **Fig. 3**, located on the flow plane and cross-sectional plane of profiles formed by forward and sideways extrusion respectively, were selected for EBSD characterisation. **Fig. 13** shows the inverse pole figure (IPF) maps and grain boundaries on the flow plane. In **Fig. 13**, ED and ND represent the extrusion direction (extrudate exiting direction) and normal direction (extrudate width direction) respectively for forward and sideways extrusion. For forward extrusion, the microstructure in the extrudate central zone F_f is relatively inhomogeneous, where both fine and coarse grains were observed, as can be seen in **Fig. 13(a)**. Specifically, the microstructure is composed of a duplex grain structure constituted from some small to medium equiaxed grains and large grains containing a substructure. The small to medium equiaxed grains are surrounded by HABs and the substructure inside the large grains consists of equiaxed subgrains with LABs. It should be noted that for common forward extrusion where the extrudate cross-section is smaller than that of the billet, elongation of grains of the extrudate along the extrusion direction was usually observed as the material experiences tension in the extrusion direction and compression in the direction perpendicular to extrusion [35, 36, 39]. In this study, as shown in **Fig. 10(e)**, for forward extrusion, tension arises along the direction Z perpendicular to extrusion, due to existence of a die pocket, as a result the grids are not obviously elongated along the

extrusion direction *Y,* as can be seen in **Fig. 7(f)**. Thus no obvious elongation of grains along the extrusion direction has been found in the profile obtained by forward extrusion.

For sideways extrusion, the microstructure in the extrudate central zone S_f is shown in **Fig. 13(b)**, where two types of structural components are evident. One is a band-like structure consisting of the coarse grains with HABs. This type of band-like structure tends to have been extensively elongated along the extrusion direction (ED) in the middle region where the flow dividing line exists. This accords with the elongated grids in the *Z* direction shown in **Fig. 8** and is attributable to the tensile strain acting in the *Z* direction when passing the die orifice, as shown in **Fig. 10(f)**. In addition, the band-like structure above and below the flow dividing line tends to have been tensioned and slightly rotated upwards and downwards to the horizontal direction, respectively. This is compatible with the upward and downward flow lines above and below the flow dividing line shown in **Fig. 8**, caused by tensile and shear deformation in the intersection region, as shown in **Fig. 10(f)** and **(h)**. The other structural component is made up of essentially equiaxed grains with a large number of LABs (subgrains) and few HABs within the band-like structure. The band-like structure in the upper and lower region, where both shearing and tension exist, is finer than that in the centre, where tension mainly exists. Also, the fraction of HABs within the band-like structure is larger in the upper and lower region than that in the centre, indicating that they have a higher degree of dynamic recrystallization due to shearing. It should be noted that both extruded profiles were immediately cut off and quenched in water, the effect of static recrystallization and recovery is rather limited. The static recrystallization is likely to occur for the remaining extrudate within the die and leads to a relatively higher fraction of HABs.
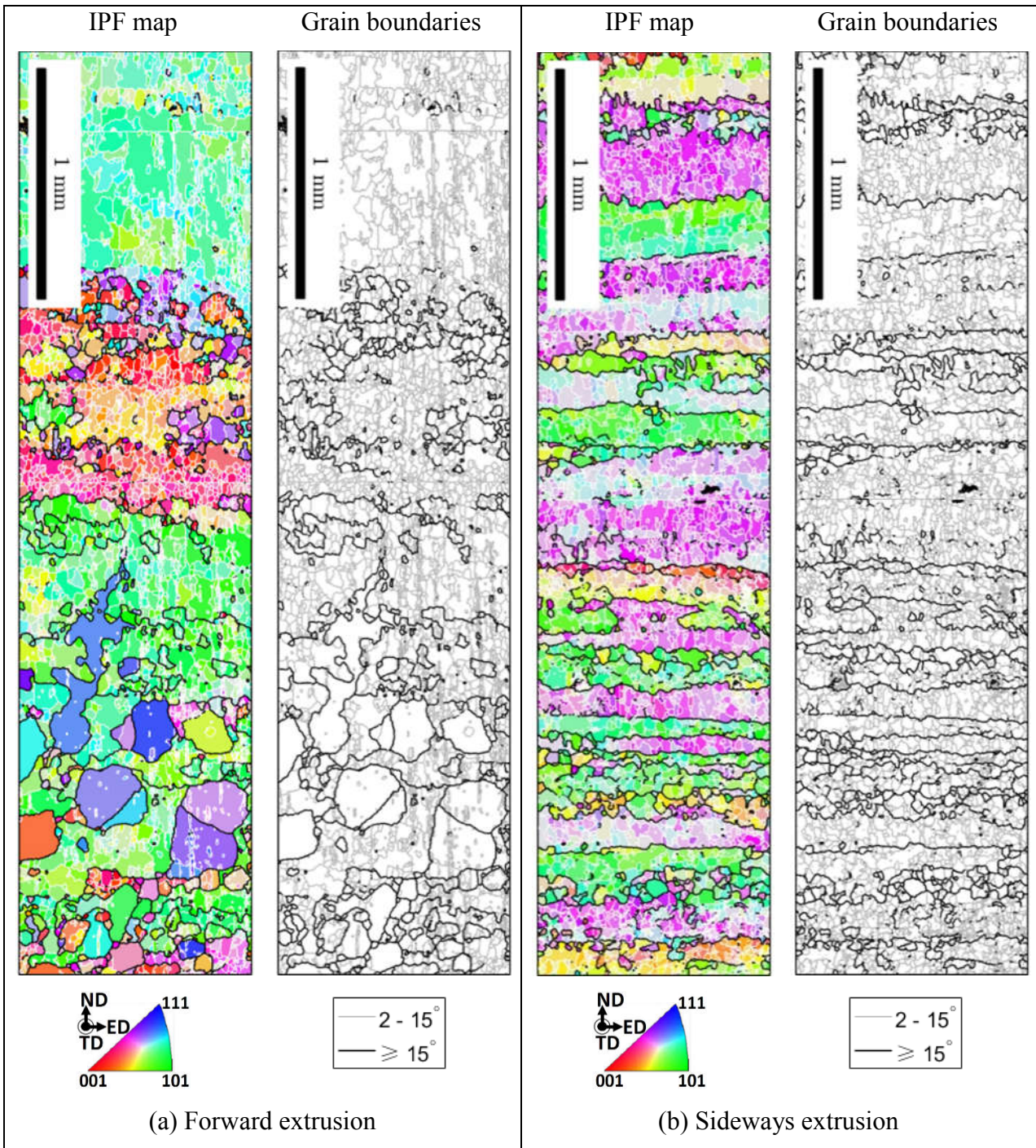
Fig. 13. EBSD inverse pole figure (IPF) maps and grain boundaries at zones F_f and S_f on the flow plane of profiles.

Fig. 14 (a) and **(b)** show the microstructure on the cross-sectional plane of profiles formed by forward and sideways extrusion, respectively. It can be seen that for both forward and sideways extrusion, grains on the surface areas have a relatively larger fraction of HABs and smaller size compared with those in the centre. This is probably due to the friction effect, which increases the shear strain. It can

also be seen that the grains are more obviously elongated along the ND direction for forward extrusion, this is due to the tension arising along the direction Z perpendicular to extrusion, as shown in **Fig. 7(f)** and **Fig. 10(e)**.
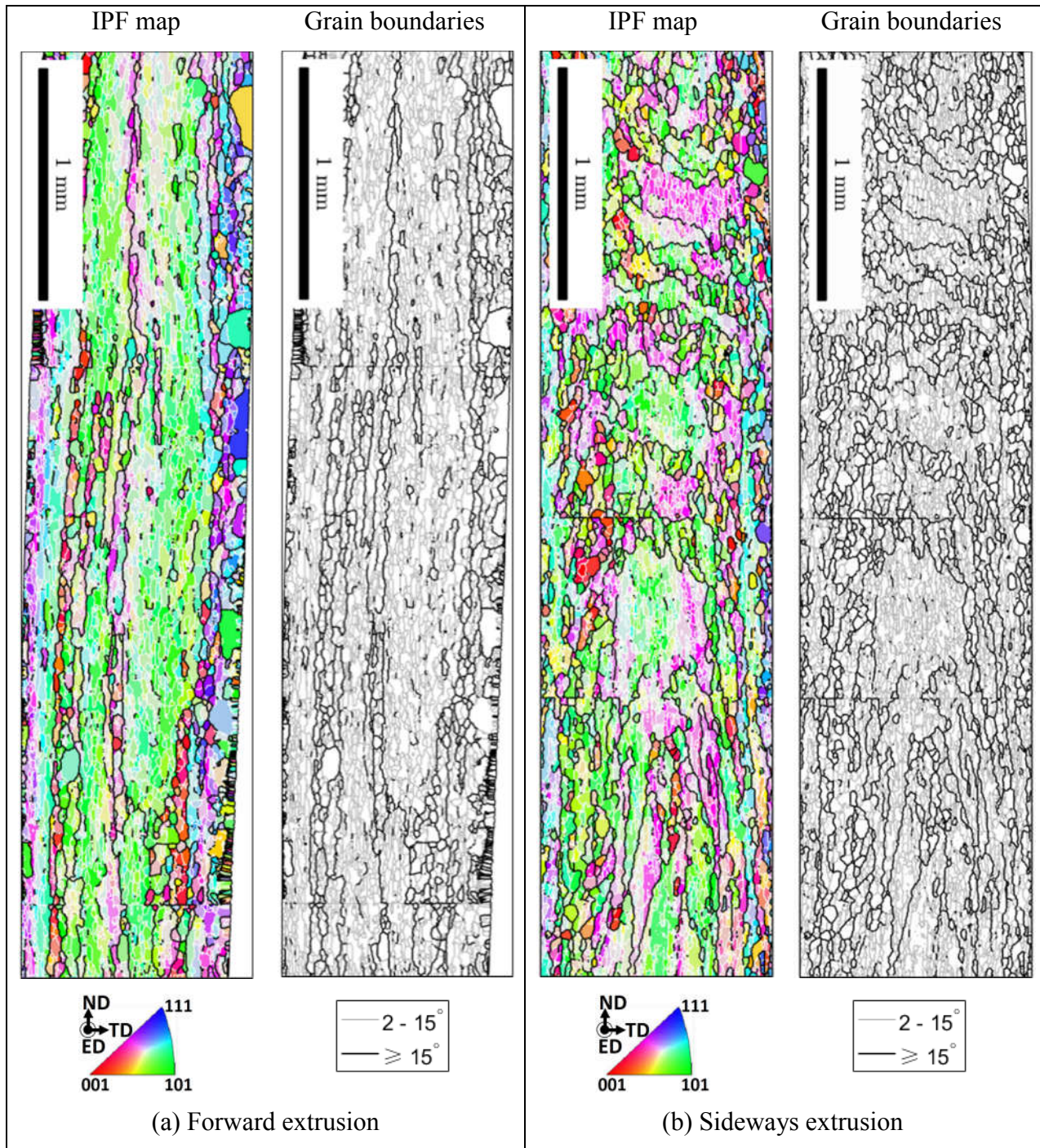

Fig. 14. EBSD inverse pole figure (IPF) maps and grain boundaries at zones F_c and S_c on the cross-sectional plane of profiles.

Quantified grain size distribution for all grains with LABs and HABs is shown in **Fig. 15(a)** and **(b)**. From these figures an average grain size of about 26 μm for forward extrusion, and about 18 μm for sideways extrusion is estimated. It can be seen that the sideways extruded profile has a smaller average grain size, due to relatively greater effective strain leading to greater grain refinement. However, it is obvious from **Figs. 13-14** that most of the grains in both the sideways and forward extruded profiles are subgrains with LABs. **Fig. 16** shows the misorientation angle distribution for zones F_f, Fc and S_f, Sc in the formed profiles. Fractions of grain boundaries between 2-10° and 2-15° have been calculated for forward and sideways extrusion. Generally, a lower fraction of grain boundaries with misorientation angles less than 10° or 15° exists in the cross-sectional plane than that in the flow plane, due to the increased shear deformation in the surface caused by friction. The sideways extruded profile has a slightly higher fraction of grain boundaries with low misorientation angles less than 10°. For forward extruded profile, the misorientation angle distribution in both planes has a peak value at a low angle around 5°. Compared with forward extrusion, the misorientation angle distribution in both planes of the sideways extruded profile is relatively non-uniform, with a lower peak value at around 2°.
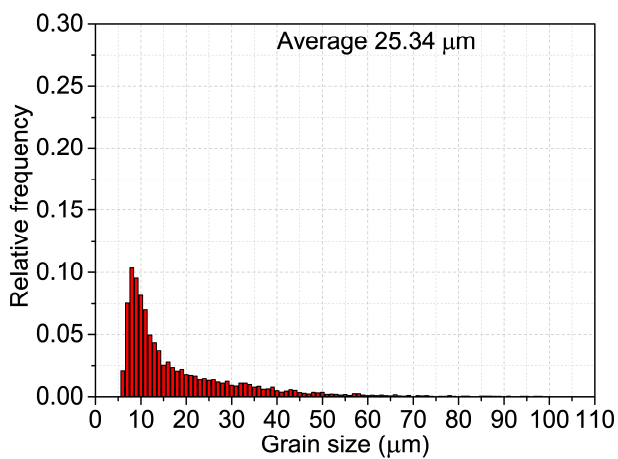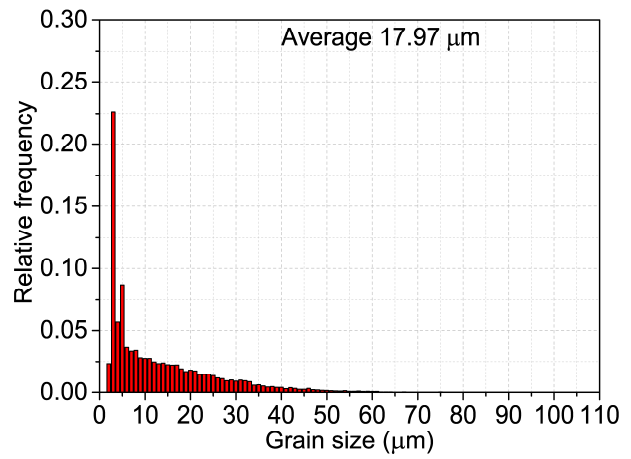

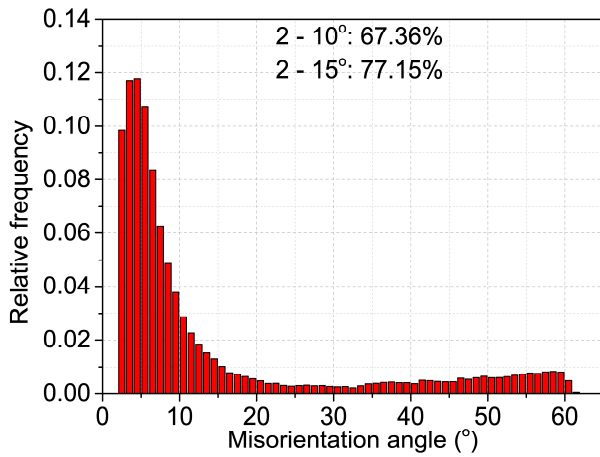(a) Forward extrusion - flow plane   (b) Sideways extrusion - flow plane
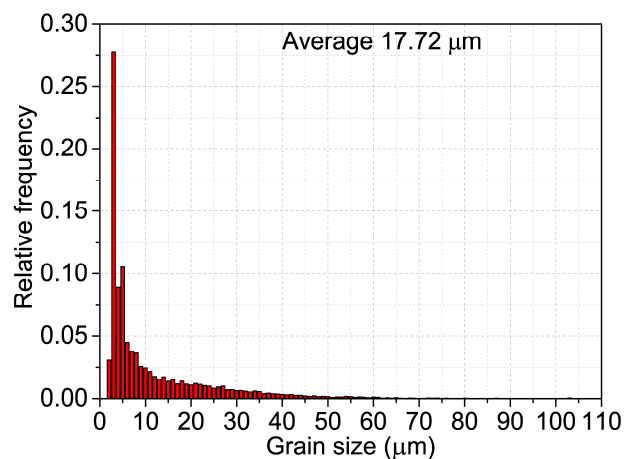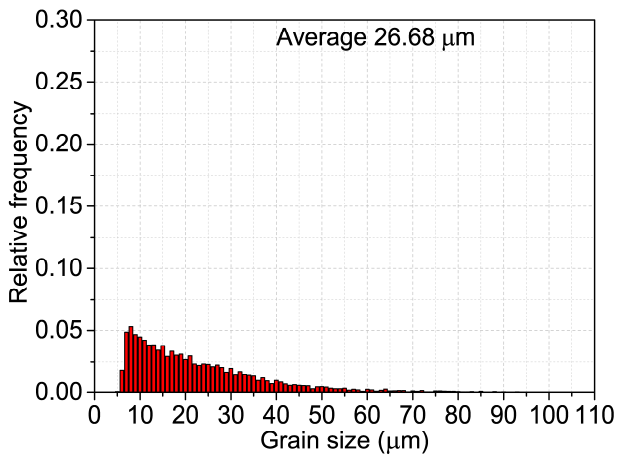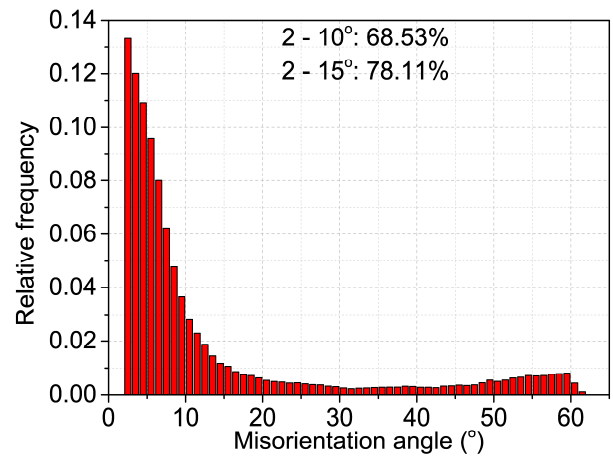
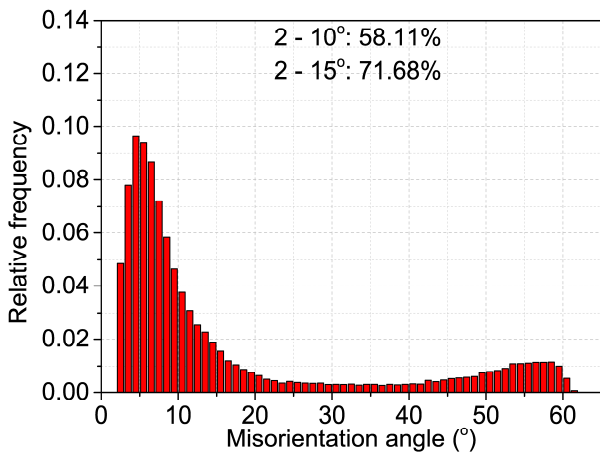(c) Forward extrusion – cross-sectional plane   (d) Sideways extrusion – cross-sectional plane

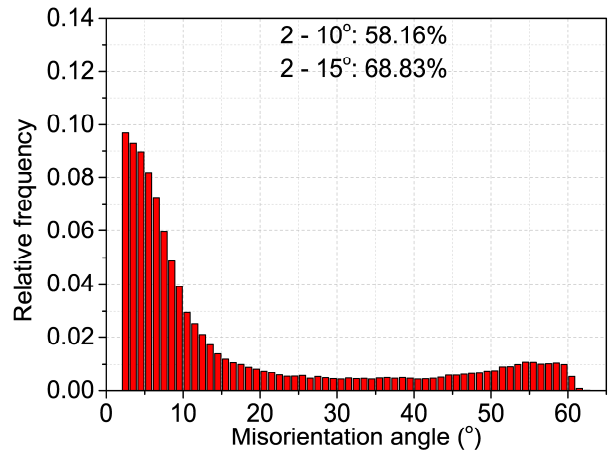**Fig. 15.** Grain size distribution at zones F_f, F_c and S_f, S_c of profiles.

(a) Forward extrusion - flow plane   (b) Sideways extrusion - flow plane

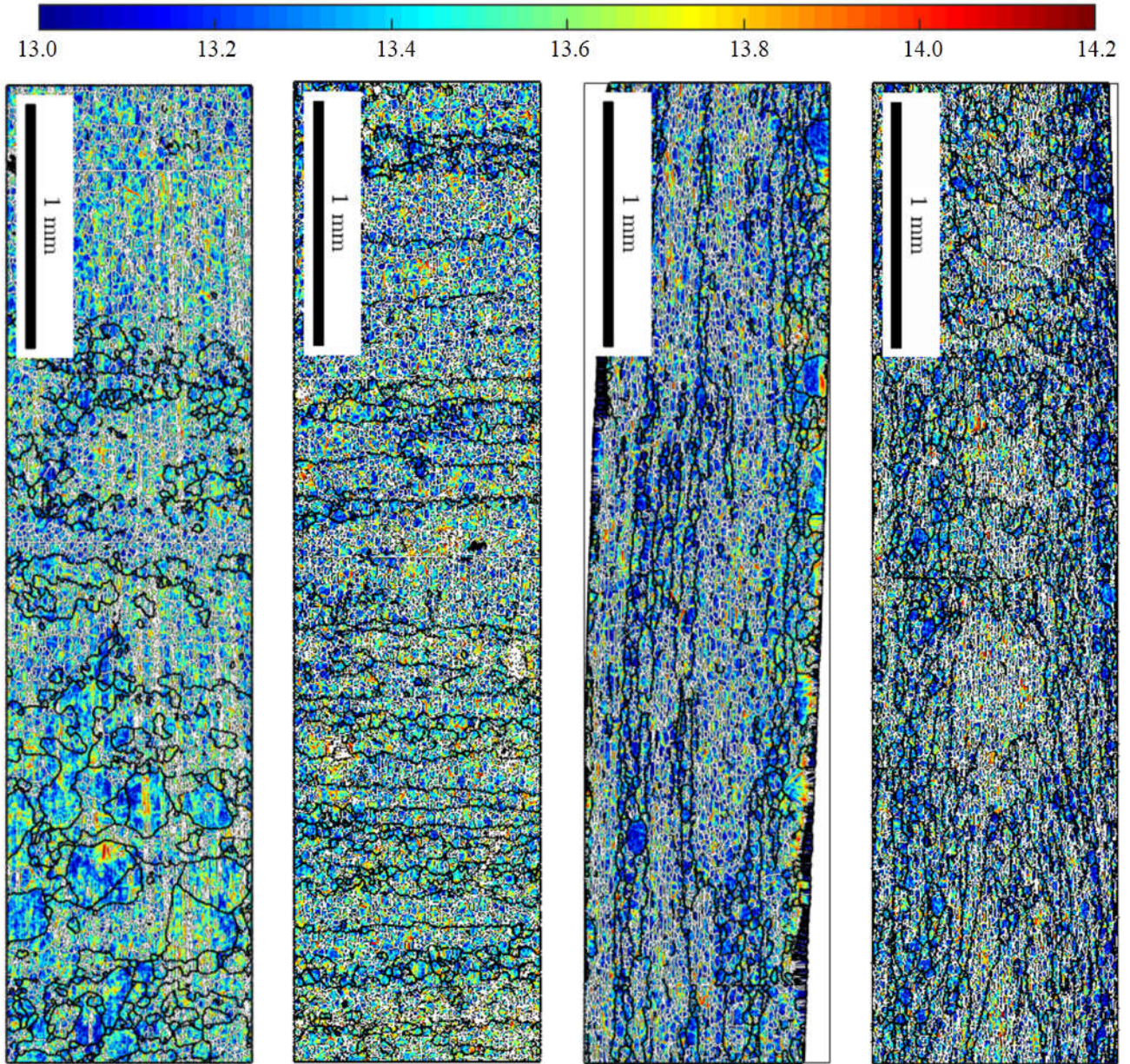(c) Forward extrusion - cross-sectional plane   (d) Sideways extrusion - cross-sectional plane

Fig. 16. Misorientation angle distribution at zones F_f, F_c and S_f, S_c of profiles.

In general, for metals deformed at moderate strain rates and at temperatures above approximately half that of their melting point ($T > 0.5T_m$, T_m is the melting point in Kelvin), such as hot extrusion, hot

rolling, and hot forging, plastic deformation occurs by dislocation motion where both strain hardening, strain rate hardening and dynamic recovery exist. New grains are generated during deformation as a result of dynamic recrystallization (DRX). For metals with high stacking fault energy (SFE) (e.g. Al, β-Ti, and ferritic steels), dynamic recovery occurs easily with annihilation and rearrangement of dislocations either by 'build' into new LABs, or absorption into the pre-existing boundaries. Also, geometrically necessary boundaries with increasing misorientation develop. These boundaries accommodate the deformation between neighbouring grains, and the related dislocations are termed geometrically necessary dislocations (GNDs) due to necessity for the geometric accommodation. These dislocations are gradually absorbed by subgrains with LABs to form recrystallized refined grains with HABs during the DRX process. The GND density maps at zones F_f, Fc and S_f, Sc of profiles obtained by forward and sideways extrusion, are shown in **Fig. 17**. The profile obtained by forward extrusion has a slightly lower GND density in both the flow plane and cross-sectional plane than that produced by sideways extrusion. This indicates that DRX is less complete in sideways extrusion where fewer dislocations are being absorbed by LABs to generate HABs. This might be attributed to the different deformation time and temperature fields associated with the two processes. Deformation at higher temperature and/or lower strain rate may provide additional driving force to cause transformation of LABs to HABs and induce more DRX. It should be noted that the temperature rise of the aluminium during deformation could attribute to coarsening of grains during straining where DRX occurs. As can be seen in the temperature field shown in **Fig. 10(k)** and **(l)**, there is little difference between temperature fields in profiles formed by forward and sideways extrusion. Therefore, the effect of temperature rise can be ruled out. However, **Fig. 10(i)** and **(j)** indicate that deformation time is greater for forward extrusion than sideways extrusion. The sideways extrusion process is a double action extrusion process where the flow dividing line is in the centre for equal speeds of upper and lower punches, thus the extrudate exit velocity is double that for forward extrusion. As deformation time is halved and temperature is virtually the same, less DRX occurred in sideways extrusion than in forward extrusion, leading to higher GND density. It should also be noted

that the GND density in the flow plane is slightly greater than that in the cross-sectional plane for both forward and sideways extrusion. This result accords with the lower fractions of LABs found in the cross-sectional plane, as indicated by **Fig. 16**.


| (a) Forward extrusion - flow plane | (b) Sideways extrusion - flow plane | (c) Forward extrusion - cross-sectional plane | (d) Sideways extrusion - cross-sectional plane |

Fig. 17. GND density maps at zones F_f, Fc and S_f, Sc of profiles. The colour scales are $\log_{10}$ scale, unit m^{-2}.

Fig. 18(a) and **(b)** show the {111} pole figure of zones F_f and S_f on the flow plane of profiles formed by forward and sideways extrusion respectively. **Fig. 19** shows the corresponding orientation

distribution function (ODF) sections of $\varphi_2 = 45^\circ$. As can be seen in **Fig. 18(a)**, the texture of the forward extruded profile is more scatteredly distributed and has a lower maximum intensity of 8.06. **Fig. 18(b)** shows that the sideways extruded profile has a more intensified distribution of texture component with a greater maximum intensity of 9.49. According to the key {111} pole figures [51] and ODF sections [52, 53] showing locations of the ideal orientations of main texture components for FCC materials, the profile formed by forward extrusion has a rolling-type texture mostly composed of the Brass {011}<211>) component and a slight Cube ({001}<100>) component, while the profile formed by sideways extrusion has a strong A-type shear texture ({111}<110>) component and a slight A_2^* ({111}<112>) component. In addition, the overall texture of the sideways extruded profile exhibits a rotation of about 5° around the TD axis (perpendicular to the flow plane ED-ND), this can be ascribed to the effect of shearing in sideways extrusion which has also been identified in ECAE/P [53] and our previous study [33]. During the simple-shear type process such as ECAE/P, {111} slip plane and <110> slip direction tend to align parallel to the shear plane and shear direction respectively due to shearing. The shearing in sideways extrusion occurs in a way similar to ECAE/P, leading to the formation of the simple shear texture. Most of the grains have the same orientation as the slip system {111}<110> of FCC materials. Hence, grains in sideways extruded thin-walled profiles (strips) are well oriented for further deformation, and the limited grain boundary rotations caused by this shear texture may effectively prevent the occurrence of fracture [54], although other factors may have an opposite effect. The texture of the forward extruded profile contains Cube component, the average Lankford parameter of which is rather small compared with {111} fibre, which may potentially lead to a low resistance to thinning in the thickness direction during further deformation such as bending and drawing [54].

(a) Forward extrusion   (b) Sideways extrusion
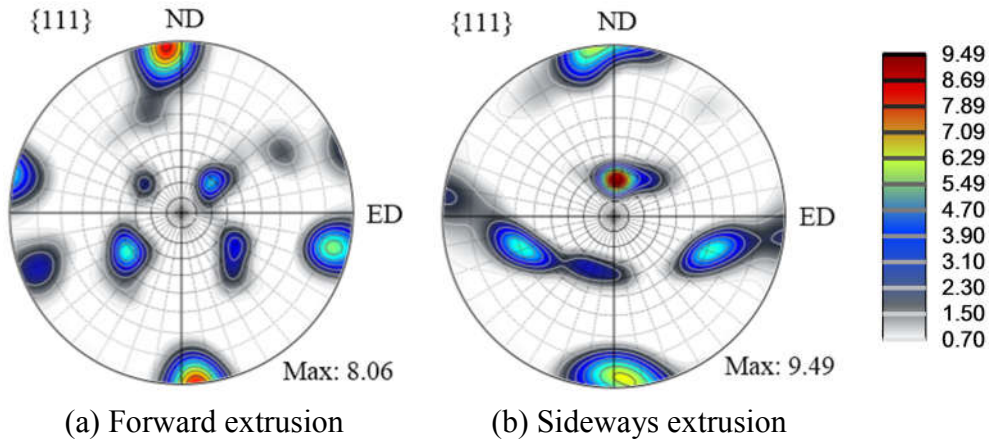
Fig. 18. The $\{111\}$ pole figures at zones F_f and S_f on the flow plane of profiles.
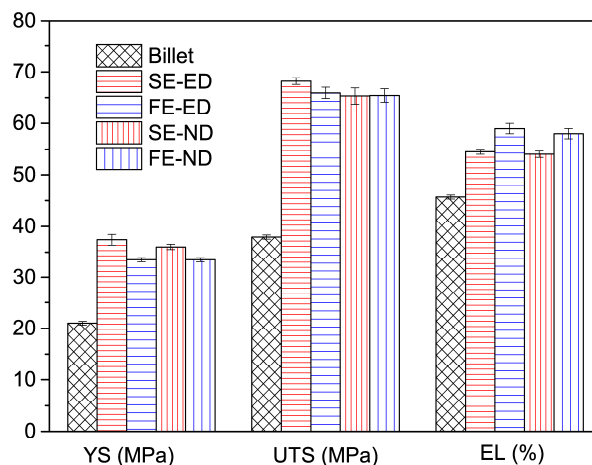

(a) Forward extrusion

(b) Sideways extrusion
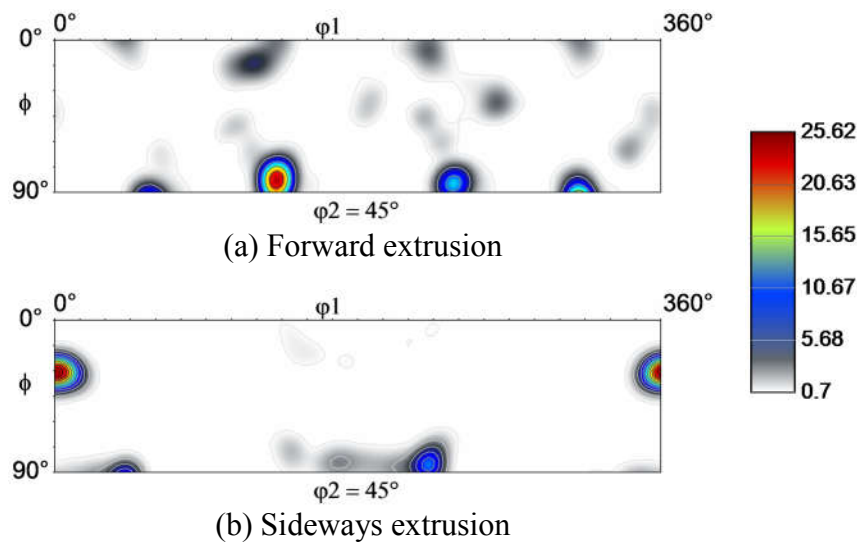
Fig. 19. The orientation distribution function (ODF) sections of $\varphi_2 = 45°$ at zones F_f and S_f on the

flow plane of profiles.

3.3.2. Tensile properties

The 0.2% proof stress (yield strength YS), ultimate tensile strength (UTS) and elongation to fracture (EL) obtained from the tensile tests are shown in **Fig. 20**. As shown in **Fig. 20**, in the extrusion direction (ED), the formed profiles obtained from both forward extrusion and sideways extrusion have an increased YS (~60% and 79%), UTS (~74% and 80%) and EL (~29% and 19%) compared to that of the billet; this is due to grain refinement. It is worth noting that both the strength and ductility of the sideways extruded profile at 480 ºC have been improved in the present study, while the profile extruded at room temperature in previous study has a decrease in ductility [33]. This could be related

to the fact that a relatively lower GND density was formed in the profile extruded at 480 ºC. The sideways extruded profile has a higher YS and UTS but a relatively lower EL than the forward extruded profile; this is attributed to the combined effects of smaller grains and higher GND density and texture intensity. The Schmid factor at the two zones F_f and S_f, taken from the flow plane of both forward and sideways extruded profiles, has also been calculated and the average value of the former, 0.422 is greater than the latter, 0.384, which conforms to the lower YS found in the forward extruded profile [55]. **Fig. 20** also shows the tensile test results in the normal direction (ND). It can be seen that the strength in ND is slightly lower than that in ED, the difference in strength is slightly more obvious for sideways extrusion. This is probably due to the significantly elongated grain morphology in ED for sideways extrusion. It should be noted that in the current work, for extruding profiles with a very large width using a small diameter extrusion press/billet, an extra pocket in the forward extrusion is designed. The spreading die pocket design results in preform in the pocket, which is expected to lead to increased effective strains and thus enhanced grain refinement compared with conventional forward extrusion without a die pocket. Therefore, sideways extrusion may have more significant improvement in strength compared with conventional forward extrusion without a die pocket. This will be figured out in the future work.

Fig. 20. Mechanical properties of the billet and extrusion profiles (SE-sideways extrusion, FE-forward extrusion).

It should also be noted that the basic deformation rules of our sideways extrusion process is in essence affected by the different velocity ratios of the two opposing punches for a given die orifice design. The effect of the velocity ratio on the location of the line (**Fig. 6c**) dividing the deformation zone in extrusion container and die orifice has been studied in previous work [32, 47, 48]; basically, the dividing line would slightly deviate from the centre (0.5) to the lower velocity side (~ 0.7) depending on the velocity ratio of the two punches, but the deformation mechanism (flow patterns) and the elongated grain morphology would not be radically changed. Future work needs to be carried out specially focusing on sideways extrusion with different velocity ratios, temperatures and strain rates to study their effects on microstructure and mechanical properties.

4. Conclusions

Wide thin-ribbed Z-shaped aluminium profiles were formed by novel sideways extrusion and conventional forward extrusion at the same temperature (480 ºC) and speed (0.1 mm/s). Finite element process modelling was conducted to investigate the different deformation mechanisms and aspects of extrusion load, flow pattern, strain field, strain rate field, and temperature field. Microstructure characterisation and tensile tests were carried out to compare the resulting microstructure and mechanical properties. The following conclusions are drawn from the results:

(1) Although a die pocket can be designed to reduce the diameter of the billet and container of the extrusion press needed for forward extrusion of wide profiles, it results in a greater peak extrusion force than that of sideways extrusion, due to the die design with a die pocket leading to upsetting (preform, ~ 2 times spread of billet diameter) before extrusion. Two dead metal zones (DMZs) of right triangular shapes have been identified in the 90 degree corners of the die pocket opposite the die orifice for forward extrusion, while a DMZ of roughly triangular shape exists in the billet on the chamber wall opposite and central to the die orifice for sideways extrusion.

(2) For forward extrusion with a spreading die pocket, relatively uniform compressive strains are generated in the central zone of the die pocket in the extrusion direction (ED), while tensile strains

exist along the normal direction (ND) perpendicular to extrusion. After passing the die orifice, compressive strains in ED turn into tensile strains, and tensile strains in ND further increase, leading to relatively equiaxed elongated grids in both ED and ND. Also, shear exists above and below the work-piece centre zone in the intersection zone of the billet and die pocket. Sideways extrusion mainly generates shear strains in zones above and below the mid-width flow dividing line, while tensile strains in ED dominate on the dividing line, leading to greatly elongated grids in ED. Although the die pocket leads to preform for forward extrusion, it results in smaller effective strains in the thin rib than that of sideways extrusion.

(3) In the region with an equal effective strain, shear strain is more effective in increasing the average misorientation angle and promoting grain refinement than normal strain components. Sideways extrusion results in a larger fraction of subgrains with smaller sizes in the central rib than that obtained by forward extrusion, because of greater effective strains. Greatly elongated grains with a band-like structure along ED were observed in sideways extrusion, which were not found in forward extrusion due to the die pocket design leading to tensile strains perpendicular to the extrusion direction. Compared with the extrusion condition of 480 ℃ and 0.1 mm/s, higher extrusion temperature or slower extrusion speed favourable for DRX needs to be considered for improving the grain refinement in sideways extrusion.

(4) Sideways extrusion results in a higher yield strength (YS) and ultimate tensile strength (UTS) but a slightly lower elongation to failure (EL) due to the combined effects of grain refinement, GND and texture intensity enhancement. Anisotropy was slightly more obvious for sideways extrusion due to the existence of band-like grain structure. In comparison with the billet, the YS and UTS of the profile in ED have been improved by ~ 60% and ~ 74% for forward extrusion, and ~ 79% and ~ 80% for sideways extrusion, respectively, indicating that the sideways extrusion process is more advantageous to improve material strength under the same extrusion condition.

References

[1] W.J. Joost, Reducing Vehicle Weight and Improving U.S. Energy Efficiency Using Integrated Computational Materials Engineering, JOM 64 (2012) 1032-1038.

[2] J.M. Allwood, C.F. Dunant, R.C. Lupton, C.J. Cleaver, A.C.H. Serrenho, J.M.C. Azevedo, P.M. Horton, C. Clare, H. Low, I. Horrocks, J. Murray, J. Lin, J.M. Cullen, M. Ward, M. Salamati, T. Felin, T. Ibell, W. Zhou, W. Hawkins, Absolute zero: Delivering the UK's climate change commitment with incremental changes to today's technologies, UK FIRES (2019).

[3] A.E. Tekkaya, N.B. Khalifa, G. Grzancic, R. Hölker, Forming of Lightweight Metal Components: Need for New Technologies, Procedia Eng. 81 (2014) 28-37.

[4] F. Vollertsen, A. Sprenger, J. Kraus, H. Arnet, Extrusion, channel, and profile bending: A review, J. Mater. Process. Technol. 87 (1999) 1-27.

[5] F. Paulsen, T. Welo, A design method for prediction of dimensions of rectangular hollow sections formed in stretch bending, J. Mater. Process. Technol. 128 (2002) 48-66.

[6] H. Li, H. Yang, M. Zhan, Z. Sun, R. Gu, Role of mandrel in NC precision bending process of thin-walled tube, Int. J. Mach. Tool. Manuf. 47 (2007) 1164-1175.

[7] O. Hasegawa, K. Manabe, T. Murai, Stretch press bending of AZ31 magnesium alloy extruded square tube, Procedia Eng. 81 (2014) 2184-2189.

[8] H. Li, H. Yang, F.F. Song, M. Zhan, G.J. Li, Springback characterization and behaviors of high-strength Ti–3Al–2.5V tube in cold rotary draw bending, J. Mater. Process. Technol. 212 (2012) 1973-1987.

[9] A.A. El-Domiaty, A.A. Elsharkawy, Stretch-bending analysis of U-section beams, Int. J. Mach. Tool. Manuf. 38 (1998) 75–95.

[10] H. Yang, H. Li, Z. Zhang, M. Zhan, J. Liu, G. Li, Advances and Trends on Tube Bending Forming Technologies, Chinese J. Aeronaut. 25 (2012) 1-12.

[11] S. Chatti, M. Hermes, M. Kleiner, Three-dimensional bending of profiles by stress superposition, Springer Verlag, Berlin, 2007.

[12] M. Hermes, D. Staupendahl, M. Kleiner, Torque superposed spatial bending, Springer Verlag, Berlin, 2015.

[13] X. Guo, H. Xiong, H. Li, Y. Xu, Z. Ma, A.A. El-Aty, Y. Ma, K. Jin, Forming characteristics of tube free-bending with small bending radii based on a new spherical connection, Int. J. Mach. Tool. Manuf. 133 (2018) 72-84.

[14] J. Ma, T. Welo, Analytical springback assessment in flexible stretch bending of complex shapes, Int. J. Mach. Tool. Manuf. 160 (2021) 103653.

[15] C. Lin, G. Chu, L. Sun, G. Chen, P. Liu, W. Sun, Radial hydro-forging bending: A novel method to reduce the springback of AHSS tubular component, Int. J. Mach. Tool. Manuf. 160 (2021) 103650.

[16] H. Yang, H. Li, J. Ma, G. Li, D. Huang, Breaking bending limit of difficult-to-form titanium tubes by differential heating-based reconstruction of neutral layer shifting, Int. J. Mach. Tool. Manuf. 166 (2021) 103742.

[17] A. Selvaggio, D. Becker, A. Klaus, D. Arendes, M. Kleiner, Curved Profile Extrusion, Springer Verlag, Berlin, 2015.

[18] K.B. Müller, Bending of extruded profiles during extrusion process, Int. J. Mach. Tool. Manuf. 46 (2006) 1238-1242.

[19] M. Shiraishi, M. Nikawa, Y. Goto, An investigation of the curvature of bars and tubes extruded through inclined dies, Int. J. Mach. Tool. Manuf. 43 (2003) 1571-1578.

[20] J.J. Tiekink, Extrusion method and extrusion apparatus, US5305626A, 1992.

[21] Y.P. Wang, F. Li, X.W. Li, Effect of extrusion ratio (λ) on dynamic recrystallization of AZ31 magnesium alloy bending products prepared by staggered extrusion (SE), Int. J. Adv. Manuf. Technol. 108 (2020) 289-297.

[22] C. Etherington, CONFORM—a new concept for the continuous extrusion forming of metals, J. Eng. Ind. 96 (1974) 893-900.

[23] C. Wick, J.T. Benedict, E.F. Veilleux, Cold and warm extrusion, in: Tool and Manufacturing Engineers Handbook, fourth ed., Society of Manufacturing Engineers, Dearborn, USA, 1983.

[24] V. Segal, Equal-Channel Angular Extrusion (ECAE): From a Laboratory Curiosity to an Industrial Technology, Metals 10 (2020) 244.

[25] G.J. Raab, R.Z. Valiev, T.C. Lowe, Y.T. Zhu, Continuous processing of ultrafine grained Al by ECAP–Conform, Mater. Sci. Eng. A 382 (2004) 30-34.

[26] R. Geiger, W. Schätzle, Grundlagen und Anwendung des QuerflieBpressens [Principles and applications of transverse extrusion], in: Proceedings of the International Conference on Fundamentals of Metal Forming Technique-State and Trends, Stuttgart, October 1983, pp. 139-160

[27] S. Rudolf, Hollow lateral extrusion of tubular billets-a newly developed cold forging process, in: 43rd plenary meeting of the International Cold Forging Group (ICFG), Darmstadt, Germany, 2010.

[28] M. Merklein, Cold Forging, in: L. Laperrière, G. Reinhart (Eds.) CIRP Encyclopedia of Production Engineering, Springer Verlag, Berlin, 2014, pp. 226-231.

[29] J. Wälder, M. Liewald, Hollow lateral extrusion of tubular billets-Further development of the cold forging process, Applied Mechanics and Materials 794 (2015) 160-165.

[30] R. Balendra, Y. Qin, Identification and classification of flow-dependent defects in the injection forging of solid billets, J. Mater. Process. Technol. 106 (2000) 199-203.

[31] G. Winiarski, A. Gontarz, G. Samołyk, Flange formation in aluminium alloy EN AW 6060 tubes by radial extrusion with the use of a limit ring, Archives of Civil and Mechanical Engineering 19 (2019) 1020-1028.

[32] W. Zhou, J. Lin, T.A. Dean, L. Wang, Feasibility studies of a novel extrusion process for curved profiles: Experimentation and modelling, Int. J. Mach. Tool. Manuf. 126 (2018) 27-43.

[33] W. Zhou, J. Yu, J. Lin, T.A. Dean, Manufacturing a curved profile with fine grains and high strength by differential velocity sideways extrusion, Int. J. Mach. Tool. Manuf. 140 (2019) 77-88.

[34] M. Chandrasekaran, Y.M.S. John, Effect of materials and temperature on the forward extrusion of magnesium alloys, Mater. Sci. Eng. A 381 (2004) 308-319.

[35] C. Zhang, C. Wang, Q. Zhang, G. Zhao, L. Chen, Influence of extrusion parameters on microstructure, texture, and second-phase particles in an Al-Mg-Si alloy, J. Mater. Process. Technol. 270 (2019) 323-334.

[36] A. Güzel, A. Jäger, F. Parvizian, H.G. Lambers, A.E. Tekkaya, B. Svendsen, H.J. Maier, A new method for determining dynamic grain structure evolution during hot aluminum extrusion, J. Mater. Process. Technol. 212 (2012) 323-330.

[37] S.-w. Bai, G. Fang, J. Zhou, Integrated physical and numerical simulations of weld seam formation during extrusion of magnesium alloy, J. Mater. Process. Technol. 266 (2019) 82-95.

[38] S. Kaneko, K. Murakami, T. Sakai, Effect of the extrusion conditions on microstructure evolution of the extruded Al–Mg–Si–Cu alloy rods, Mater. Sci. Eng. A 500 (2009) 8-15.

[39] X. Chen, G. Zhao, G. Liu, L. Sun, L. Chen, C. Zhang, Microstructure evolution and mechanical properties of 2196 Al-Li alloy in hot extrusion process, J. Mater. Process. Technol. 275 (2020) 116348.

[40] G. Fang, J. Zhou, J. Duszczyk, Effect of pocket design on metal flow through single-bearing extrusion dies to produce a thin-walled aluminium profile, J. Mater. Process. Technol. 199 (2008) 91-101.

[41] I. Duplancic, M. Mioc, Z. Bracic, Case Studies on Control of Metal Flow in Pre-Chamber Dies, in: Proceedings of the Seventh International Aluminum Extrusion Technology Seminar, Chicago, Illinois, 2000.

[42] G. Fang, J. Zhou, J. Duczczyk, X.K. Wu, FE Simulation of Extrusion to Produce a Thin-Walled Wide Profile through a Spreading Pocket Die, Key Engineering Materials 367 (2008) 63-70.

[43] Q. Li, C.J. Smith, C. Harris, M.R. Jolly, Finite element investigations upon the influence of pocket die designs on metal flow in aluminium extrusion, J. Mater. Process. Technol. 135 (2003) 189-196.

[44] D. Lesniak, W. Libura, Extrusion of sections with varying thickness through pocket dies, J. Mater. Process. Technol. 194 (2007) 38-45.

[45] Users manual, QForm 9.0.

[46] N. Biba, S. Stebunov, A. Vlasov, Material forming simulation environment based on QForm 3D software system, in: 12th International Conference on Metal Forming 2008, pp. 611-616.

[47] W. Zhou, J. Lin, T.A. Dean, L. Wang, Analysis and modelling of a novel process for extruding curved metal alloy profiles, Int. J. Mech. Sci. 138-139 (2018) 524-536.

[48] W. Zhou, J. Yu, J. Lin, T.A. Dean, Effects of die land length and geometry on curvature and effective strain of profiles produced by a novel sideways extrusion process, J. Mater. Process. Technol. 282 (2020) 116682.

[49] Y. Iwahashi, J. Wang, Z. Horita, M. Nemoto, T.G. Langdon, Principle of equal-channel angular pressing for the processing of ultra-fine grained materials, Scr. Mater. 35 (1996) 143-146.

[50] D.N. Lee, An upper-bound solution of channel angular deformation, Scr. Mater. 43 (2000) 115-118.

[51] J.A. Muñoz, M. Avalos, R.E. Bolmaro, Heterogeneity of strain path, texture and microstructure evolution of AA6063-T6 processed by Equal Channel Angular Sheet Extrusion (ECASE), J. Alloys Compd. 768 (2018) 349-357.

[52] J. Yu, G. Zhao, C. Zhang, L. Chen, Dynamic evolution of grain structure and micro-texture along a welding path of aluminum alloy profiles extruded by porthole dies, Mater. Sci. Eng. A 682 (2017) 679-690.

[53] I.J. Beyerlein, L.S. Tóth, Texture evolution in equal-channel angular extrusion, Prog. Mater. Sci. 54 (2009) 427-510.

[54] X. Bai, High-Shear Deformation Processing on Aluminum Alloy for Sheet Production, in: School of Materials Engineering, Purdue University, West Lafayette, Indiana, 2018.

[55] R. Zhang, Z. Xu, L. Peng, X. Lai, M.W. Fu, Modelling of ultra-thin steel sheet in two-stage tensile deformation considering strain path change and grain size effect and application in multi-stage microforming, Int. J. Mach. Tool. Manuf. 164 (2021) 103713.